FINAL REPORT

Kalman Filters for UXO Detection: Real-Time Feedback and Small Target Detection

SERDP Project MR-2106

MAY 2012

Tomasz M. Grzegorczyk
Delpsi LLC

Benjamin E. Barrowes
ERDC-CRREL

This document has been cleared for public release

SERDP
DOD ▪ EPA ▪ DOE

This report was prepared under contract to the Department of Defense Strategic Environmental Research and Development Program (SERDP). The publication of this report does not indicate endorsement by the Department of Defense, nor should the contents be construed as reflecting the official policy or position of the Department of Defense. Reference herein to any specific commercial product, process, or service by trade name, trademark, manufacturer, or otherwise, does not necessarily constitute or imply its endorsement, recommendation, or favoring by the Department of Defense.

Contents

Acronyms **v**

Keywords **vi**

Acknowledgments **vii**

Abstract **viii**
1. Background . . . viii
2. Objectives . . . viii
3. Summary of Science/Technology . . . ix
4. Summary of results . . . ix
5. Conclusions and implications for future research . . . x

1 Introduction **1**

2 Kalman filters: background and validation **4**
1. Review of filters implementation . . . 4
2. Application to UXO detection . . . 7
3. Iterative KF-EKF algorithm . . . 11

3 Validation with the MPV-II sensor **13**
1. The sensor . . . 13
2. Dynamic mode . . . 13
3. Results . . . 16
4. An alternative formulation . . . 20

4 Validation with the MetalMapper sensor **23**
1. The sensor . . . 23
2. Results from KF-EKF . . . 24
3. Note on processing time . . . 29
4. Graphical User Interface proposal . . . 33

Conclusions and future work **35**

Bibliography **37**

List of Tables

2.1 Reference configurations for various sensors and inverted positions using the Gauss-Newton method of [Grzegorczyk 11] and the Extended Kalman Filter (EKF) where polarizabilities are known. All dimensions are given in centimeters. 9

2.2 KF-EKF iterative algorithm for the estimation of UXO position $\bar{r}'$, orientation (θ,ϕ), and time dependent diagonal polarizability tensor $\bar{\bar{\beta}}(t)$. 12

4.1 Mean and standard deviations (in centimeters) of the positions obtained by (1) the KF-EKF algorithm compared to the Gauss-Newton (GN) reference and (2) the KF-EKF algorithm compared to the results provided by G&G Sciences Inc.. The sample size is of 55 targets over 10 dynamic lanes at Camp San Luis Opbispo, each lane being about 60 m in length. 29

List of Figures

2.1 Evolution of the estimated positions (x, y, z) with the measurement sequence from synthetic dynamic MetalMapper data. Initial guesses for examples 1 and 2 are $(-29, 0, -12)$ [cm] and $(-20, -20, -6)$ [cm] for a final answer at $(-34, -2, -49)$ [cm]. 6

2.2 Kalman filter prediction of a single dipole for synthetic measurement data: (a) noiseless case; (b) original data to which Gaussian noise has been added of zero mean and variance equal to 20% of the maximum value of the magnetic field. The true values of the dipole are $\bar{m} = (2, 0.2, 0.2)$, $\bar{r} = (10, 20, -40)$ cm. . . . 8

2.3 Kalman filter prediction of the position of a single dipole source located at $\bar{r} = (10, 20, -40)$ cm and of dipole moment $\bar{m} = (2, 0.2, 0.2)$. 9

2.4 Posterior probability density function (right) obtained from the initial Gaussian distribution (left) after applying the extended Kalman filter. The final *pdf* is non-Gaussian as expected. The initial and final means and variances are: $\bar{r}^{ini}_{mean} = (20, 0, -30)$ cm and $\sigma^{ini} = (0.1, 0.1, 0.1)$; $\bar{r}^{end}_{mean} = (0, 0, -61.5)$ cm and $\sigma^{end} = (0.02, 0.3, 0.01)$. 10

2.5 Inversion results of position and polarizabilities when sequentially processed by an iterative algorithm. The state is initially far from the ground truth and presents a reasonable accuracy after 10 iterations. 11

3.1 Photographs of the MPV-II sensor, comprising a boom for hand-held maneuverability at the end of which is located the EMI head. The latter is composed of a circular transmitter (49.68 cm diameter) and five equi-spaced cubic receivers (8 cm side). 14

3.2 Field values and their average (solid black line) from a series of dynamic measurements centered over a 20 mm target. 15

3.3 Polarizability of three UXO (see insets) from static data measured by the MPV-II. The 2.7 ms limit of dynamic data collection is indicated. The reference gray signatures are based on a Gauss-Newton inversion [Grzegorczyk 11]. 17

3.4 Evolution of position estimates in the (xy) plane as the filter is updated for various transmitter positions. The random initial guesses, between -1 m and $+1$ m in the (xy) plane, are indicated by the green circles and the final estimated positions are indicated by the blue crosses. The ground truths are indicated by red squares. The gray paths illustrate the sequential estimates during the iterative process. 18

3.5 Same as Figure 3.4 with initial guesses between -0.5 m and $+0.5$ m. 19

3.6 Comparison between field components collected atop an off-centered 20-mm UXO in a static mode (solid lines) truncated at 2.7 ms and a dynamic mode (dashed lines). 20
3.7 Polarizabilities of a 20-mm UXO obtained from dynamic MPV-II measurements. The reference gray signatures are based on a Gauss-Newton inversion [Grzegorczyk 11]. 21
3.8 Polarizabilities obtained by an iterative KF-EKF sequential algorithm from MPV-II data collected over a 57-mm UXO. The reference gray signatures are based on a Gauss-Newton inversion [Grzegorczyk 11]. The inverted positions are $(4, -5, -42)$ cm and $(0, -3, -41)$ cm obtained with the KF-EKF and GN algorithms, respectively, whereas the ground truth is listed as $(0, 0, -35)$ cm to the tip of the vertical-nose-up 57-mm. 22

4.1 Geometry of the MetalMapper used in the algorithm. The primary field coil dimensions are 1 m $\times$ 1 m and produce a magnetic field computed from the addition of four wires supporting the same constant current. For computational efficiency, the received field is computed at the center of each receiver only, i.e. the finite size of the receiving cubes is not accounted for. 25
4.2 Target picks from dynamic data collected at Camp Butner, NC. The background represents the interpolated $\log_{10}$ values of the H_z component at the central receiver. The color scale is chosen to produce red and blue regions at location of strong and weak magnetic field values, respectively. 27
4.3 Inverted positions around a Northing position of 31.5 m in Figure 4.2. 28
4.4 Comparison between G&G Sciences Inc.target picks (blue circles) and KF-EKF algorithm target picks (red crosses) for Camp San Luis Obispo dynamic MetalMapper data. 30
4.5 Comparison between the averaged polarizabilities obtained by G&G Sciences Inc. (blue line) and by the KF-EKF algorithm (red line) across all target picks. . . . 31
4.6 Newly implemented KF-EKF algorithm with three different settings, yielding three different data processing times. The figures show a history of estimated positions as the MetalMapper drives by a target. 32
4.7 Snapshot of the GUI and results obtained from the processing of dynamic lane 33 at Camp Butner. Results are obtained with the KF-EKF algorithm and show the predicted positions in the (xy) plane, the predicted depth, the inverted polarizabilities with a related aspect ratio of the UXO, and a detection metric based on a linear fit of the polarizabilities. 34

Acronyms

CA	:	California
EKF	:	Extended Kalman Filter
EMI	:	Electromagnetic Induction
ERDC	:	Engineer Research and Development Center
GN	:	Gauss-Newton
GPS	:	Global Positioning System
GPU	:	Graphics Processing Unit
GUI	:	Graphical User Interface
IEEE	:	Institute of Electrical and Electronics Engineers
ISO	:	Industry Standard Objects
KF	:	Kalman Filter
MPV	:	Man-Portable Vectorial
MR	:	Munition Response
MTADS	:	Multi-sensor Towed Array Detection System
NC	:	North Carolina
Rx	:	Receiver
RTK	:	Real-Time Kinematic
SERDP	:	Strategic Environmental Research and Development Program
SLO	:	San Luis Obispo
SNR	:	Signal to Noise Ratio
TEMTADS	:	Time-domain Electro-Magnetic MTADS
Tx	:	Transmitter
UXO	:	Unexploded ordnance

Keywords

- Bayes' rule
- Electromagnetic induction
- Extended Kalman filters
- UXO detection
- Dipole model
- Dynamic data collection
- Gauss-Newton algorithm
- Geophysical signal processing
- Kalman filters
- MetalMapper sensor
- MPV-II sensor
- Real-time detection
- Static data collection
- Subsurface sensing
- TEMTADS sensor
- Unexploded ordnance

Acknowledgments

The work reported here on Kalman filters for UXO detection was supported by the Strategic Environmental Research and Development Program, under project # MR-2106. The principal investigator was Dr. Tomasz M. Grzegorczyk of Delpsi LLC whose main focus was to implement the method and validate it on measurement data from the MPV-II and MetalMapper new generation sensors. The co-performer was Dr. Benjamin E. Barrowes of the U.S. Army Corps of Engineers, Engineer Research and Development Center (ERDC), Hanover Site. Dr. Barrowes was responsible for collecting static and dynamic data with the MPV-II sensor. Although he did so on multi-target configurations, the scope of this project limited ourselves to single-target configurations. We also acknowledge the help of Dr. Dave George of G&G Sciences Inc. who provided us with dynamic data from the MetalMapper sensor. These data were collected at former Camp San Luis Obispo (CA) and Camp Butner (NC).

Abstract

1. Background

Improvement in the detection and discrimination of UXO using the EMI regime has been consistent during the last two decades, in both instrument hardware and detection software. There is nonetheless still a disparity between the often idealized environments considered ("golf course" situation) and the reality in the field. Working on diminishing this disparity, various SERDP programs focus on developing versatile (next generation) instruments as well as robust software for data processing in realistic environments, yielding ever improved classification performance.

The current protocol for surveying fields is typically organized in two stages. First the sensors are used in a survey mode, or *dynamic mode*, collecting data over large areas and flagging locations which may be contaminated by a subsurface UXO. The flagging process is typically based on magnetic field amplitude, based on the rationale that high amplitudes may correspond to buried UXO and should therefore be further investigated. Hence, at the second stage, the sensors return to the locations of interest for more in depth data collection in order to feed the identification and classification algorithms with high quality and diverse data. Flagging based on field amplitude, however, has potential drawbacks: the magnetic field in the EMI regime decays fast and a deep UXO may not produce a strong response while still being potentially hazardous.

2. Objectives

The purpose of this SEED project is to investigate an alternative method to flag areas of interest at the first stage of data collection with the following objectives:

- Work with dynamic data – Dynamic data are typically more noisy and less diverse than cued interrogation data (collected at the second stage). The method should therefore be tolerant to noise and able to provide inversion results with such a reduced dataset.

- Provide position and polarizability estimates – We wish to go beyond the field plot and better identify the targets, in order to make more informed decisions on the probability of presence of targets of interest. The output of the method should therefore include target position in the (xy) plane for subsequent data collection if necessary, target depth to still potentially flag deeper UXO, and target polarizabilities to have a first identification procedure and not miss deep UXO or small items.

- Real-time processing – The method should not slow down the survey speed and should therefore work in real-time while still satisfying the two constraints above. For purpose of practicality, we set our real-time limit to 100 ms, which is the rate at which dynamic data are currently acquired by sensors such as the MPV-II and the MetalMapper.

- Applicability to small items – The method should be validated on multiple UXO including some challenging ones such as 20-mm projectiles.
- Validation with next generation sensors – Actual data from dynamic measurements should be used as the ultimate validation of the method.

3. Summary of Science/Technology

The approach proposed by this work is to implement an algorithm based on Kalman filters (KF) and Extended Kalman filters (EKF) for the sequential processing of data as they become available. Kalman filters have been developed as a stochastic signal processing technique using Bayes rule in order to filter a signal out of a well characterized noise. Kalman filters, however, only provide an optimal minimum mean square error estimator if some constraints are satisfied. We supposed throughout the report that these constraints are satisfied: all noise sources can be drawn from a Gaussian distribution as well as prior probability density functions related to the unknown parameters to be estimated. Kalman filters also require the parameters to be linear with measurements: within the dipole approximation often used to process EMI data, this condition is satisfied by the dipole moment $\bar{m}(t)$ which can be directly related to the polarizability tensor $\bar{\bar{\beta}}(t)$. The position, however, appears as a non-linear parameter which we estimate using the extended Kalman filter and a linearization of the equations. Finally, both algorithms (KF and EKF) are iterated to sequentially process the data and yield converged values of all parameters to be estimated.

4. Summary of results

The main achievement of this SEED project is the implementation and validation of an iterative KF-EKF approach satisfying all conditions above: dynamic data processing, inversion of all the parameters of the dipole model, and real-time processing. In addition, the validation has been performed on various targets, including a small 20-mm item which remains a challenging target to identify. The validation of the KF-EKF iterative algorithm has been performed on all next generation sensors available to us: TEMTADS, MPV, MPV-II, and MetalMapper. For practicality purposes, we have concentrated on the last two sensors since the TEMTADS is usually not used for dynamic surveys and since the MPV-II is currently replacing the MPV.

It is worth mentioning that the purposes of dynamic data collections with the MPV-II and the MetalMapper are very different in our investigation. The MPV-II, meant for hand-held operation, was used to interrogated a limited area within which a single target was present, akin to being waved by an operator in a detection mode. The MetalMapper instead was driven along adjacent 60-m long lanes to flag target locations across a large geographical area. In this latter configuration, multiple targets were present in the underground and sequentially appeared and disappeared from the field of view of the sensor as it was driven across the area. In both cases, the sensors operated in dynamic mode, meant for rapid land survey at the expense of data quality. Despite the noisy data, the KF-EKF algorithm was able to converge to proper solutions as verified independently either using our Gauss-Newton reference algorithm, using ground truth information whenever available, or comparing with independently obtained results. In addition,

processing times of each new data collection were measured to be less than 100 ms on a regular 2×2.8 GHz Quad-Core Intel Xeon computer, which is the real-time limit for our application. The inverted parameters include position, depth, and polarizabilities, albeit limited to the short data collection time range inherent to a dynamic survey. Yet, even if this dynamic data is not sufficient to perform classification, it is often sufficient to identify the subsurface anomaly as possible UXO or not, either based on simple signal correlation to a library or based on a volume estimate. The method can therefore be used in land survey for real-time target mapping, flagging those locations to which the instrument needs to return for more exhaustive, cued interrogation, data collection.

An IEEE Transactions on Geoscience and Remote Sensing article has been submitted as the result of this project: "*Real-time processing of electromagnetic induction dynamic data for unexploded ordnance detection*", by Tomasz M. Grzegorczyk and Benjamin E. Barrowes.

5. Conclusions and implications for future research

As part of this work, a GUI was proposed to display the results to an operator, showing in real time the evolution of position, depth, and polarizability estimates as new data become available during the measurement process. Combining this information, an indication on target aspect ratio, a volume estimate, and the likelihood of being a target of interest are also displayed on the GUI. Such an integrated tool could be a useful feature to implement on existing sensors and taken on-board during field surveys. Future work in this direction would include:

1. Integration to existing on-board softwares with sensors of interest
2. Extensive validation in various terrain configurations
3. Optimization of feedback information (probability of target, library matching, volume estimation)
4. Extension to new sensors (in particular Pedemis [Barrowes 12])
5. Use of an 8 ms dynamic window (instead of the current 2.7 ms) to provide considerably improved identification possibilities since the KF-EKF algorithm achieves more than just detection

1. Introduction

The detection and discrimination of unexploded ordnance (UXO) remains an important environmental and engineering challenge which has attracted much attention for the last two decades. Accomplishments reported from both hardware and software point of views have moved the research focus from simple laboratory tests to much more complex environments, accompanied by instruments and inversion algorithms adapted to ever more realistic terrains. This trend is for example illustrated by the recent evolution of electromagnetic induction (EMI) instruments toward ever improved versatility and accuracy. From the GEM family [Won 99] to TEMTADS [Nelson 07, Nelson 01], MPV [Fernández 11], and Metal Mapper [Prouty 09b], the instruments have gained properties such as efficiency, portability, vectorial excitation, vectorial reception, etc. The transmitter and receivers are often mounted on the same sensor and are therefore co-located [Nelson 07, Prouty 09b, Fernández 11], although recent sensors attempt to decouple the transmitter and receiver location for broader coverage and more diverse information content [Barrowes 12]. Cart-mounted instruments have the important advantage of providing consistent measurements from transmitter to transmitter, and can measure either a single component of the magnetic field (e.g. TEMTADS) or all three components (e.g. MetalMapper). Their disadvantage, however, comes from the fact that these sensors cannot be deployed in challenging terrains where vegetation or surface state are non trivial. For these cases, hand-held instruments such as the MPV are more desirable and open the possibility of surveying areas of difficult access.

Accompanying hardware improvements, increasingly more sophisticated algorithms have been developed. Common to most methods is the inversion, either sequential or simultaneous, of the intrinsic characteristics of the targets (polarizabilities) and of their position $\bar{r}$. It has been recognized that the inversion of $\bar{r}$ is more challenging and often requires the solution of an ill-conditioned system. Various methods have been proposed to address this problem, from direct optimization based on analytical methods [Zhang 01], model-based approaches [Miller 01], statistical approaches [Tantum 01], expansions into spheroidal and/or ellipsoidal modes [Barrowes 04, Chen 07, Grzegorczyk 08], to more direct approaches based on scalar and vector potentials [Shubitidze 08]. The dipole moment $\bar{m}$, on the other hand, is easier to compute once the position is known, and can be obtained either at every time channel (or every frequency if such instruments are used) or following a parametrized equation [Pasion 07]. More recent works have proposed a simultaneous inversion of both parameters, yielding methods that have been applied to the inversion of multiple targets present in the field of view of the sensor [Song 09, Grzegorczyk 09, Grzegorczyk 11], akin to multi-UXO configurations or to UXO in the presence of a few but large clutter items.

The fast field decay in the EMI regime and the depths at which UXO are typically buried (usually 10 cm or more) results in negligible near-field effects at the receiver level so that the

secondary field is well approximated by that of a dipole [Jackson 99, Bell 01, Zhang 03]:

$$\bar{H}(\bar{r},t) = \frac{1}{4\pi|\bar{r}|^3}\left(\frac{3\bar{r}(\bar{r}\cdot\bar{m}(t))}{|\bar{r}|^2} - \bar{m}\right), \tag{1.1a}$$

$$= \frac{1}{4\pi|\bar{r}|^3}\left(\frac{3\bar{r}\bar{r}}{|\bar{r}|^2} - I\right)\cdot\bar{m}(t), \tag{1.1b}$$

where $\bar{r} = \bar{r}_{\mathrm{Rx}} - \bar{r}'$ is the distance between the receiver at position $\bar{r}_{\mathrm{Rx}}$ and the dipole modeling the UXO at position $\bar{r}'$. The dipole moment $\bar{m}(t)$ is related to the intrinsic polarizabilities of the target $\bar{\bar{\beta}}(t)$ [Bell 01] by a rotation about the target angles $\bar{\bar{R}}(\theta,\phi)$ weighted by the primary field at location $\bar{r}'$:

$$\bar{m}(t) = \bar{\bar{R}}^T(\theta,\phi)\,\bar{\bar{\beta}}(t)\,\bar{\bar{R}}(\theta,\phi)\,\bar{H}^{pr}(\bar{r}_{\mathrm{Tx}} - \bar{r}') \tag{1.2a}$$

$$\text{where} \qquad \bar{\bar{\beta}}(t) = \begin{pmatrix} \beta_x(t) & 0 & 0 \\ 0 & \beta_y(t) & 0 \\ 0 & 0 & \beta_z(t) \end{pmatrix} \tag{1.2b}$$

In order to simplify the notation, we omit the dependence of $\bar{m}(t)$ on the transmitter position $\bar{r}_{\mathrm{Tx}}$ and write $\bar{m}(\bar{r}_{\mathrm{Tx}} - \bar{r}', t) = \bar{m}(t)$. The polarizabilities $\bar{\bar{\beta}}(t)$ are intrinsic features of the target, independent on position and orientation, and can therefore be used for classification purposes. Various techniques have been proposed to estimate the parameters $(\bar{r}', \theta, \phi, \bar{\bar{\beta}}(t))$, from physics-based inversions [Shubitidze 08], deterministic approaches [Pasion 01b, Pasion 07, Grzegorczyk 11], to statistical approaches [Collins 02, Pulsipher 04, Aliamiri 07]. All these methods have been shown to yield accurate parameter estimation in various configurations, from single to multi-target, and can therefore be used to feed identification methods [Pasion 01a, Tantum 01, Shubitidze 10, Kappler 11, Beran 11a, Beran 11b, Kass 12] as well as classification methods [Fernández 10, Hu 04] with an dig/no-dig decision with a quantifiable degree of confidence.

A proper identification and classification require high quality data which in turn require a good positioning of the sensors atop the UXOs. The data collection protocol is currently based on a two-stage process: (1) target mapping, whereby the sensors are used in a detection mode to simply flag areas of interest and (2) cued interrogation whereby the sensors return to the areas of interest for more thorough data collection. At the first step, data quality is sacrificed at the profit of speed, with the purpose of surveying large areas quickly. Target mapping is currently based on field measurements, identifying regions of high amplitudes likely to correspond to actual targets. However, this procedure can be incompatible with field situations since deep targets could produce weak measured secondary field due to the strong decay in the EMI regime, yet still corresponding to hazardous items. Improved methods for target detection are therefore necessary, and proposing one such method is the purpose of the present work.

The desirable features of a detection algorithm are to provide estimates on the target location and signature, while in addition being fast in order to be compatible with a rapid land survey. A method based on correlation to a sphere signal was proposed in [George 11] and demonstrated to successfully estimate the location and depth of targets. The assumption, however, is that the three principal axes of a target respond with equal amplitude within the short time decay window measured during a dynamic survey (typically 2.7 ms). Although this is usually the case at very early time, the assumption quickly breaks down at later time channels. In this work, we return to the tri-axial dipole approximation of Eq. (1.1b) and propose a method based on an iteration between Kalman filters (KF) and Extended Kalman filters (EKF) to estimate the

parameters $\bar{m}(t)$ – hence $\bar{\bar{\beta}}(t)$ – and $(\bar{r}', \theta, \phi)$ without constraints beyond the statistics required by KF. In the following chapters, we briefly review the fundamentals of KF and EKF and apply them to both static and dynamic measured data, with a special emphasis on the MPV-II and the MetalMappersensors.

2. Kalman filters: background and validation

The notation used throughout this report is as follows: vectors and matrices appear with a bar and double bar, respectively, subscript indicate discrete realizations of a random process which we call *instance* as opposed to the more commonly used *time*, in order not to introduce possible confusion with the actual time decay of the magnetic field as the eddy currents diffuse into the targets. Although this real time decay could be used within the Kalman filter framework we formulate subsequently (because of the assumption of time-invariant UXO position and orientation angles), we refrain from doing so simply because of the nature of the sensors we use which provide the entire measured time decay of the measured magnetic fields all at once and not sequentially.

1. Review of filters implementation

Kalman filters have been developed as a stochastic signal processing technique using Bayes' rule in order to filter a signal out of a well characterized noise. Although they are an important generalization over Wiener filters in that they can accommodate vector signals and noises which may not be stationary (which are properties of interest to us in the realm of UXO detection), Kalman filters only provide an optimal minimum mean square error estimator if some constraints are satisfied. The latter are stated in the brief review included hereafter, understanding that this review is merely meant to facilitates the comprehension of the remainder of the report and not to provide an exhaustive and mathematically complete demonstration of the underlying derivations of Kalman and Extended Kalman filters. The interested reader is referred instead to specific literature on this topic [Kalman 60, Kay 93, Gordon 02].
We start by considering a general state sequence $\{\bar{x}_k, k \in \mathbb{N}\}$ whose evolution is written as

$$\bar{x}_k = \bar{f}_k(\bar{x}_{k-1}, \bar{v}_{k-1}), \tag{2.1a}$$

where $\bar{f}_k$ is the governing function. In our case, the state vector $\bar{x}_k$ is composed of the unknowns to be determined, namely the components of the position vector or of the polarizability of the UXO. These unknowns are related to the measurements by the function $\bar{h}_k$:

$$\bar{\eta}_k = \bar{h}_k(\bar{x}_k, \bar{n}_k), \tag{2.1b}$$

the measurements being the magnetic field components collected by EMI sensors across transmitters and receivers. In Eqs. (2.1), $\{\bar{v}_{k-1}, k \in \mathbb{N}\}$ and $\{\bar{n}, k \in \mathbb{N}\}$ are independent and identically distributed process noise sequences with covariance matrices $\bar{\bar{Q}}_{k-1}$ and $\bar{\bar{R}}_k$, respectively.

The data $\bar{\eta}_k$ thus collected constitute sequential information identified by the subscript k. Our purpose is to estimate the state $\bar{x}_k$ at instance k knowing the measurements up to instance k and the state $\bar{x}_{k-1}$ at instance $(k-1)$. In other words, we need to estimate the conditional

probability density function (*pdf*) $p(\bar{x}_k|\bar{\eta}_{1,k})$, where $\{\bar{\eta}_{1,k}, k \in \mathbb{N}\}$ represents the measurement vector. This *pdf* can typically be obtained recursively in two steps: predict and update. At the prediction stage, the *pdf* $p(\bar{x}_{k-1}|\bar{x}_{1,k-1})$ is known at instance $(k-1)$ and the prior *pdf* at instance k is obtained using the Chapman-Kolmogorov equation [Gordon 02]

$$p(\bar{x}_k|\bar{\eta}_{1,k-1}) = \int d\bar{x}_{k-1}\; p(\bar{x}_k|\bar{x}_{k-1})\, p(\bar{x}_{k-1}|\bar{\eta}_{1,k-1}). \tag{2.2}$$

When measurements at instance k become available, the posterior *pdf* is obtained using Bayes' rule:

$$p(\bar{x}_k|\bar{\eta}_{1,k}) = \frac{p(\bar{\eta}_z|\bar{x}_k)\, p(\bar{x}_k|\bar{\eta}_{1,k-1})}{p(\bar{\eta}_k|\bar{\eta}_{1,k-1})}, \tag{2.3}$$

where $p(\bar{\eta}_k|\bar{\eta}_{1,k-1})$ is a normalizing constant. Kalman filters are based on the assumption that the posterior *pdf* at every step is Gaussian and as such, parametrized by a mean and a covariance matrix. This assumption holds if the conditional *pdf* at instance $(k-1)$ is Gaussian (with covariance matrix $\bar{\bar{P}}_{k-1}$), if both signal and measurement noises are drawn from a Gaussian distribution, and if $\bar{f}_k$ and $\bar{h}_k$ are linear functions of the parameters. Under these assumptions, Eqs. (2.1) are rewritten as:

$$\bar{x}_k = \bar{\bar{F}}_k \bar{x}_{k-1} + \bar{v}_{k-1}\,, \tag{2.4a}$$

$$\bar{\eta}_k = \bar{\bar{H}}_k \bar{x}_k + \bar{n}_k, \tag{2.4b}$$

which leads to the Kalman filter (KF) algorithm [Kay 93, Gordon 02]:

$$\bar{x}_{k|k-1} = \bar{\bar{F}}_k\, \bar{x}_{k-1|k-1}, \tag{2.5a}$$

$$\bar{\bar{P}}_{k|k-1} = \bar{\bar{Q}}_{k-1} + \bar{\bar{F}}_k \bar{\bar{P}}_{k-1|k-1} \bar{\bar{F}}_k^T\,, \tag{2.5b}$$

$$\bar{x}_{k|k} = \bar{x}_{k|k-1} + \bar{\bar{K}}_k(\bar{\eta}_k - \bar{\bar{H}}_k \bar{x}_{k|k-1}), \tag{2.5c}$$

$$\bar{\bar{P}}_{k|k} = \bar{\bar{P}}_{k|k-1} - \bar{\bar{K}}_k \bar{\bar{H}}_k \bar{\bar{P}}_{k|k-1}, \tag{2.5d}$$

$$\text{where}\;\; \bar{\bar{K}}_k = \bar{\bar{P}}_{k|k-1} \bar{\bar{H}}_k^T (\bar{\bar{H}}_k \bar{\bar{P}}_{k|k-1} \bar{\bar{H}}_k^T + \bar{\bar{R}}_k)^{-1}. \tag{2.5e}$$

These relations are directly applicable within the framework of the dipole approximation of Eq. (1.1b) since the dipole moment $\bar{m}(t)$ is a linear function of the magnetic field. Within the same approximation, the position and UXO orientation appear as non-linear parameters which therefore cannot be estimated using Eqs. (2.5) directly. Instead, we resort to the Extended Kalman filter (EKF), based on the linearization of the state and measurement equations. The extended Kalman algorithm is given by [Kay 93, Ristic 04]:

$$\bar{x}_{k|k-1} = \bar{f}_k(\bar{x}_{k-1|k-1}), \tag{2.6a}$$

$$\bar{\bar{P}}_{k|k-1} = \bar{\bar{Q}}_{k-1} + \hat{\bar{\bar{F}}}_k \bar{\bar{P}}_{k-1|k-1} \hat{\bar{\bar{F}}}_k^T\,, \tag{2.6b}$$

$$\bar{x}_{k|k} = \bar{x}_{k|k-1} + \bar{\bar{K}}_k(\bar{\eta}_k - \bar{h}_k(\bar{x}_{k|k-1})), \tag{2.6c}$$

$$\bar{\bar{P}}_{k|k} = \bar{\bar{P}}_{k|k-1} - \bar{\bar{K}}_k \hat{H}_k \bar{\bar{P}}_{k|k-1}, \tag{2.6d}$$

$$\text{where}\;\; \hat{\bar{\bar{F}}}_k = \left.\frac{\partial \bar{f}}{\partial \bar{x}}\right|_{\bar{x}=\bar{x}_{k-1|k-1}}, \qquad \hat{\bar{\bar{H}}}_k = \left.\frac{\partial \bar{h}}{\partial \bar{x}}\right|_{\bar{x}=\bar{x}_{k|k-1}}, \tag{2.6e}$$

$$\bar{\bar{K}}_k = \bar{\bar{P}}_{k|k-1} \hat{\bar{\bar{H}}}_k^T (\hat{\bar{\bar{H}}}_k \bar{\bar{P}}_{k|k-1} \hat{\bar{\bar{H}}}_k^T + \bar{\bar{R}}_k)^{-1}. \tag{2.6f}$$

In our implementation, however, the usual update equation (2.6d) for the covariance matrix $P_{k|k}$ is replaced by its Joseph-stabilized version [Bucy 68] in order to improve numerical stability

$$\begin{aligned} \bar{\bar{P}}_{k|k} &= \bar{\bar{M}} \cdot \bar{\bar{P}}_{k|k-1} \cdot \bar{\bar{M}}^T + \bar{\bar{K}}_k \cdot \bar{\bar{R}}_k \cdot \bar{\bar{K}}_k^T \\ \bar{\bar{M}} &= \bar{\bar{I}} - \bar{\bar{K}}_k \cdot \hat{\bar{\bar{H}}}_k. \end{aligned} \tag{2.7}$$

A convergence comparison between the two forms is illustrated in Figure 2.1 on synthetic data, where the stability of the Joseph form over the standard formulation appears clearly, as demonstrated by the much faster convergence rate of the filters.

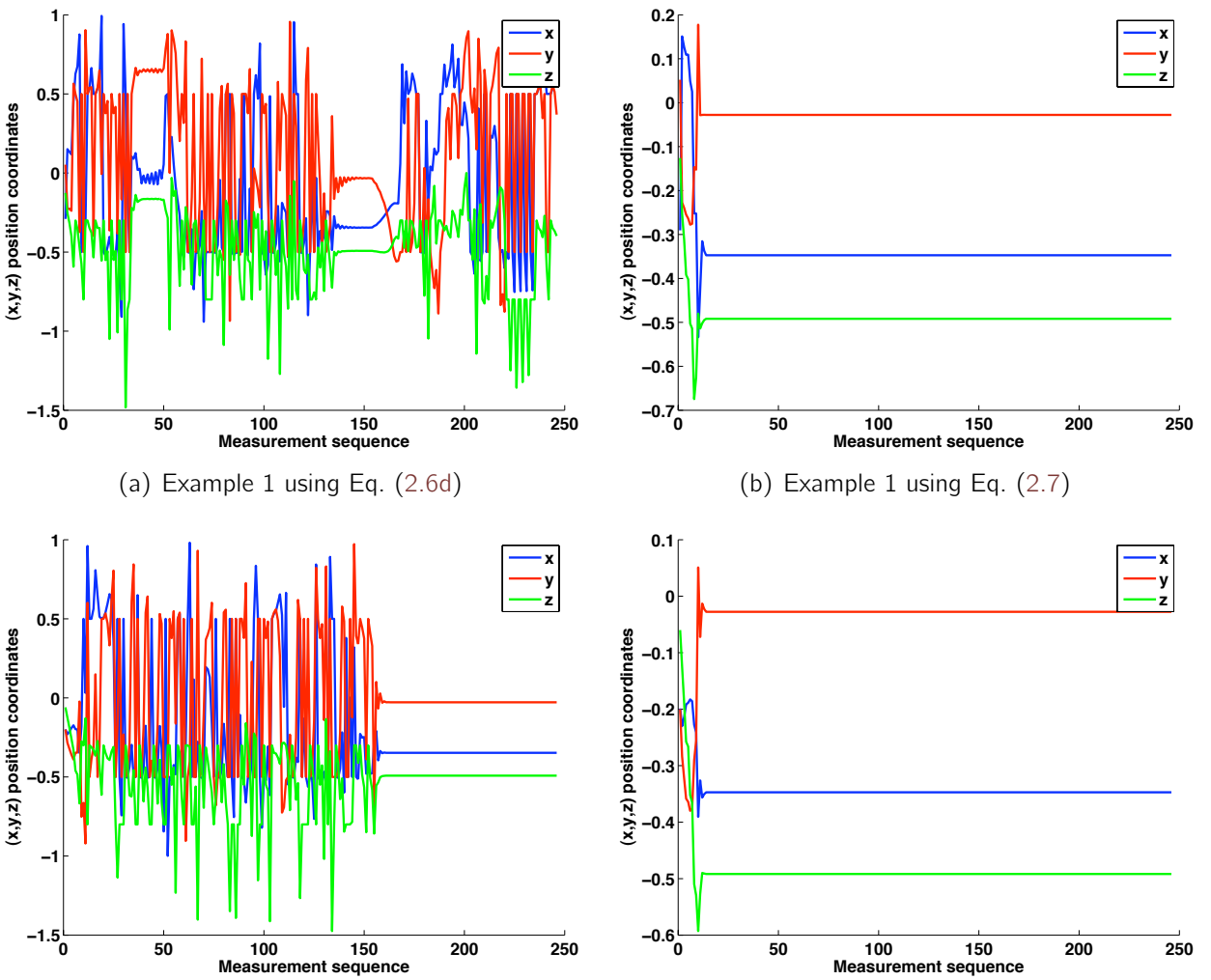

(a) Example 1 using Eq. (2.6d)

(b) Example 1 using Eq. (2.7)

(c) Example 2 using Eq. (2.6d)

(d) Example 2 using Eq. (2.7)

Figure 2.1: Evolution of the estimated positions (x, y, z) with the measurement sequence from synthetic dynamic MetalMapper data. Initial guesses for examples 1 and 2 are $(-29, 0, -12)$ [cm] and $(-20, -20, -6)$ [cm] for a final answer at $(-34, -2, -49)$ [cm].

2. Application to UXO detection

The application of Kalman filters to UXO detection is somewhat unusual because targets are stationary, which is to say that $\bar{x}_k = \bar{x}_{k-1}$ for the estimation of $(\bar{r}', \theta, \phi)$. The prediction stage can therefore be omitted. Subsequently, the two algorithms, KF of Eqs. (2.5) and EKF of Eqs. (2.6-2.7), are iteratively applied to measured data in order to sequentially estimate the positions and orientations $(\bar{r}', \theta, \phi)$ – nonlinear parameters – and the dipole moment $\bar{m}(t)$ – linear parameters – of UXO. The algorithm is detailed in Table 2.2 and reveals the iterative procedure between KF and EKF. The definitions of $\bar{x}$, $\bar{f}$, and $\bar{h}$ therefore vary with the parameters that need to be estimated. The dipole moment $\bar{m}$ is estimated with:

$$\bar{x}_k = \bar{m}_k, \tag{2.8a}$$

$$\bar{\bar{F}}_k = \bar{\bar{I}}, \tag{2.8b}$$

$$\bar{\bar{H}}_k = \frac{1}{4\pi|\bar{r}_k|^3}\left(\frac{3\bar{r}_k\bar{r}_k}{|\bar{r}_k|^2} - \bar{\bar{I}}\right), \tag{2.8c}$$

Note that $\bar{\bar{F}}_k = \bar{\bar{I}}$ is valid only at a given transmitter position, which is correct within step (1) of the algorithm of Table 2.2. The estimation of $(\bar{r}', \theta, \phi)$ supposes these parameters time independent with the following definitions:

$$\bar{x}_k = \bar{r}'_k, \quad \bar{f}_k(\bar{x}_k) = \bar{x}_k, \quad \bar{h}_k = \frac{\partial \bar{H}_k}{\partial \bar{r}'_k} \tag{2.8d}$$

$$\bar{x}_k = \phi_k, \quad \bar{f}_k(\bar{x}_k) = \bar{x}_k, \quad \bar{h}_k = \frac{\partial \bar{H}_k}{\partial \phi_k} \tag{2.8e}$$

$$\bar{x}_k = \theta_k, \quad \bar{f}_k(\bar{x}_k) = \bar{x}_k, \quad \bar{h}_k = \frac{\partial \bar{H}_k}{\partial \theta_k} \tag{2.8f}$$

where the magnetic field $\bar{H}_k$ is obtained from the dipole model of Eq. (1.1b). In practice, the three definitions of $\bar{x}$ are combined into a single vector and the corresponding $\bar{h}_k$ operator is obtained by concatenating the Jacobian matrices. The latter require the derivatives of the primary field $\bar{H}^{pr}(\bar{r})$, as seen in Eq. (1.2a), which can be computed analytically since all sensors of interest to us have either circular or square primary coils [Stratton 41, Jackson 99].

2.a Polarizability inversion

In order to validate the KF algorithm, Figure 2.2 shows inversion results of the dipole moment $\bar{m}$ in the case of synthetic data with and without noise, when the position of the dipole is known. Data are here composed of the $\hat{z}$ components of the magnetic field collected over a grid of similar extent to the TEMTADS instrument (square grid of 5×5 receivers spaced by 40 cm in both directions). The figures show the evolution of the estimated parameters (the three components of $\bar{m}$) as the sequence of data becomes available and starting from a poor initial guess. It is seen that the filter needs about seven steps to lock onto the right values in a noiseless configuration.* In a very noisy configuration and assuming that noise is well characterized, Figure 2.2(b) indicates that the filter needs more measurements but is still able to rapidly lock onto the correct values.

*Note that this results is merely an illustration of the convergence of the Kalman filter. In practise, the linear part can be directly inverted for if no noise corrupts the signal.

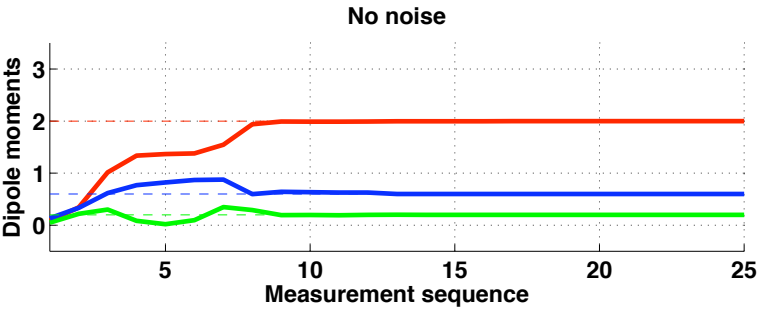

(a) Noiseless case.

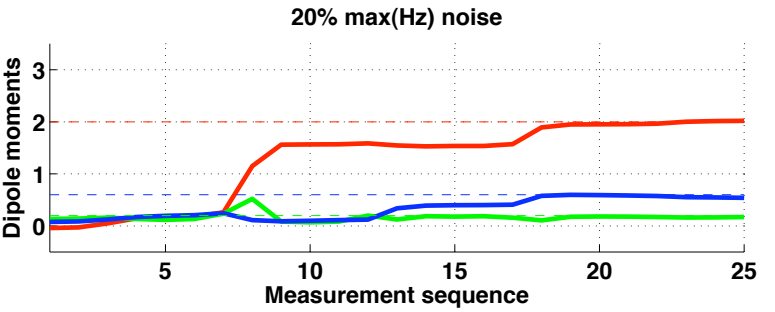

(b) 20% max(H_z) noise variance.

Figure 2.2: Kalman filter prediction of a single dipole for synthetic measurement data: (a) noiseless case; (b) original data to which Gaussian noise has been added of zero mean and variance equal to 20% of the maximum value of the magnetic field. The true values of the dipole are $\bar{m} = (2, 0.2, 0.2)$, $\bar{r} = (10, 20, -40)$ cm.

2.b Position inversion

Unlike the KF algorithm, the EKF algorithm has no optimality properties and its performance depends on the accuracy of the linearization which must be verified in our situation. Figure 2.3 provides such verification: results have been obtained using the H_z field from a single dipole at position $\bar{r} = (10, 20, -40)$ cm and moment $\bar{m} = (2, 0.2, 0.2)$ computed over a grid of 5×5 points of similar extend to the TEMTADS sensor. It should be emphasized that this result is not a demonstration but a mere verification of the applicability of the extended algorithm to our particular case (we recall that the extended Kalman filter has no optimality property). Figure 2.4 illustrates the propagation of the *pdf* through the operator, based on TEMTADS data collected above a 4.2-inch mortar. It is seen that starting from a Gaussian distribution, the final *pdf* is strongly non-Gaussian, as expected. However, its mean, computed at $\bar{r} = (0, 0, -61.5)$ cm, is in very good agreement with that obtained with a deterministic method, while its variance is relatively small.

Results obtained by the EKF algorithm are listed in the last column of Table 2.1 and reveal a few centimeter errors compared to ground truth. Interestingly, the inversions obtained from TEMTADS data are much more accurate and very stable as well as robust to noise, giving good confidence on the applicability of the EKF to position estimation.

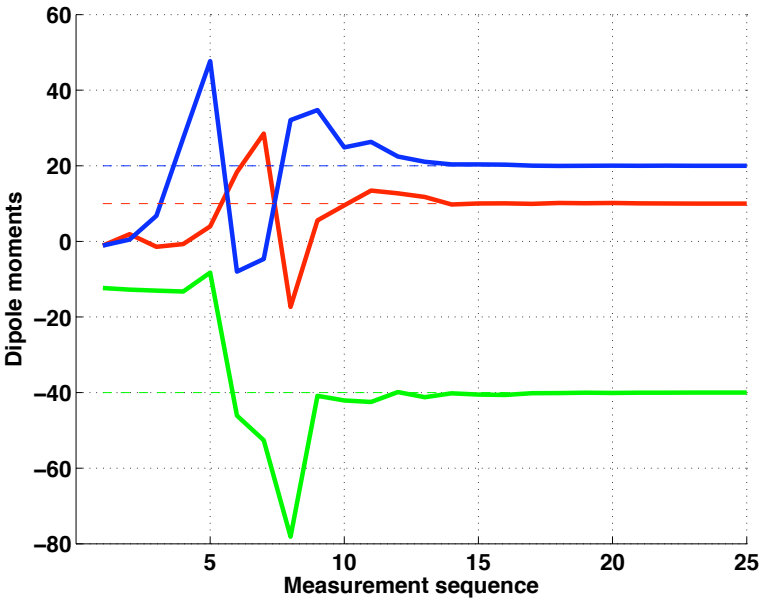

Figure 2.3: Kalman filter prediction of the position of a single dipole source located at $\bar{r} = (10, 20, -40)$ cm and of dipole moment $\bar{m} = (2, 0.2, 0.2)$.

Sensor	Configuration	Ground truth	Inversion based on [Grzegorczyk 11]	EKF Inversion
TEMTADS	4.2" mortar, horizontal	[0,0,-60]	[0,1,-61]	[3,0,-63]
	Nose piece, vertical	[0,0,-27]	[0,0,-30]	[2,0,-31]
	Half round, horizontal	[0,0,-44]	[0,1,-48]	[2,1,-49]
MPV	81-mm	[-23,22,-48]	[-15,23,-48]	[-10 18 -51]
	105-mm	[-21,22,-60]	[-13,23,-60]	[-11 21 -62]
	BLU26	[0,22,-34]	[0,22,-34]	[1 26 -38]
	57-mm	[5,22,-50]	[1,22,-50]	[0 21 -55]
	60-mm	[0,22,-46]	[0,22,-48]	[1 25 -50]
MetalMapper	Sphere	1-st quadrant	[28, 29,-36]	[25, 32,-44]
	Sphere	2-nd quadrant	[-28, 23,-35]	[-24, 25,-38]
	Sphere	3-rd quadrant	[-26,-29,-35]	[-22,-35,-39]
	Sphere	4-th quadrant	[29,-25,-36]	[38,-22,-39]
	Sphere	centered	[0, -1,-34]	[5, -7,-38]

Table 2.1: Reference configurations for various sensors and inverted positions using the Gauss-Newton method of [Grzegorczyk 11] and the Extended Kalman Filter (EKF) where polarizabilities are known. All dimensions are given in centimeters.

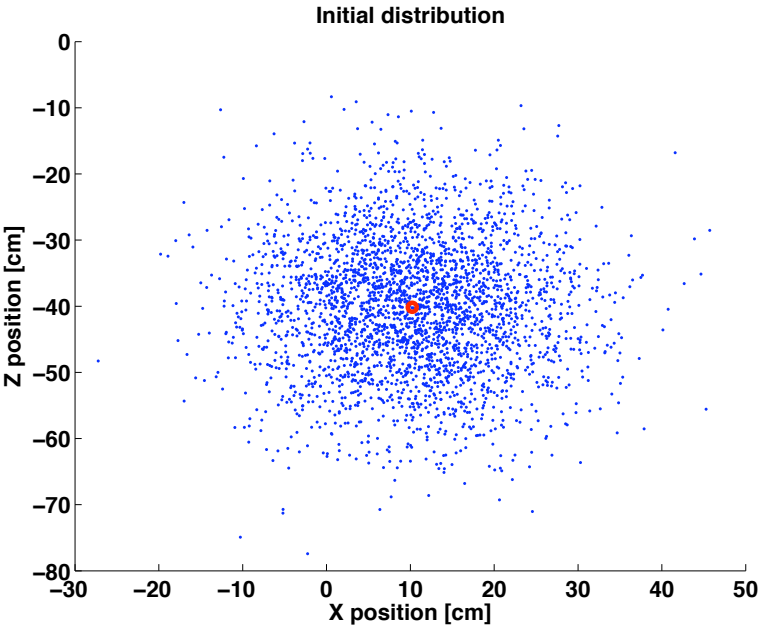

(a) Initial distribution.

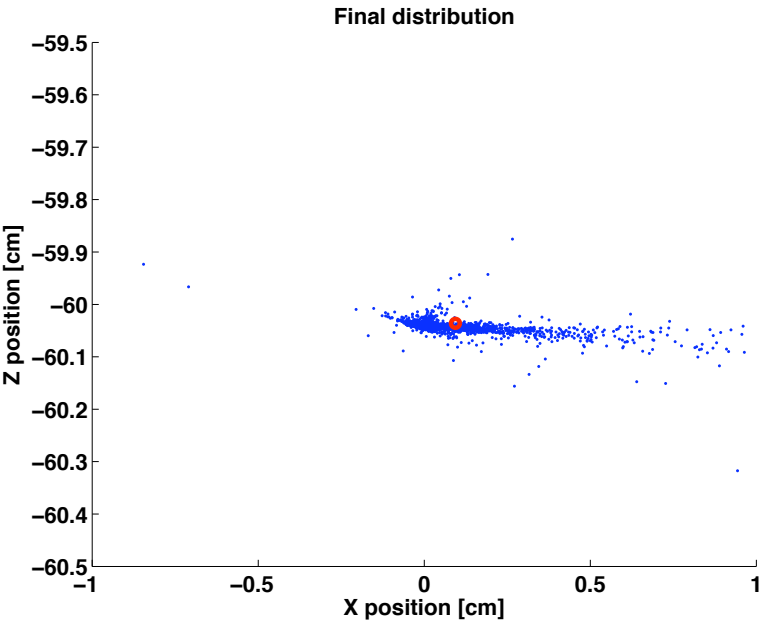

(b) Final distribution.

Figure 2.4: Posterior probability density function (right) obtained from the initial Gaussian distribution (left) after applying the extended Kalman filter. The final *pdf* is non-Gaussian as expected. The initial and final means and variances are: $\bar{r}^{ini}_{mean} = (20, 0, -30)$ cm and $\sigma^{ini} = (0.1, 0.1, 0.1)$; $\bar{r}^{end}_{mean} = (0, 0, -61.5)$ cm and $\sigma^{end} = (0.02, 0.3, 0.01)$.

2.c Simultaneous inversion of polarizabilities and position

The independent inversions of position and polarizabilities can be combined into an iterative algorithm whereby $\bar{r}$ and $\bar{m}$ are sequentially updated until a certain level of convergence is reached

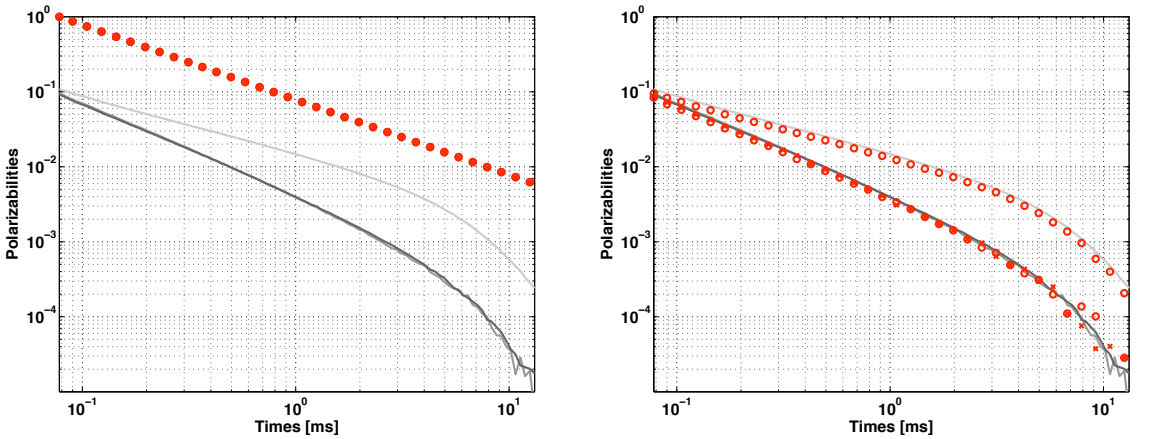

(a) Initial state: linearly decaying polarizabilities and position error of (80, 80, 60) cm in three directions.

(b) State after 10 iterations. Position error: (1.5, 0, 0.5) cm.

Figure 2.5: Inversion results of position and polarizabilities when sequentially processed by an iterative algorithm. The state is initially far from the ground truth and presents a reasonable accuracy after 10 iterations.

(typically measured by the mismatch between the computed and the measured magnetic fields). The algorithm is seeded with random means and large variances for both parameters, reflecting the fact that we have little knowledge of the final solution. Figure 2.5 shows how such algorithm performs with mortar TEMTADS data: the initial position is far from the truth and the polarizabilities are initialized to a simple linear decay. Figure 2.5(b) shows the state of the parameters after 10 iterations: the position error is reduced to a few centimeters in all three directions and the polarizabilities are well aligned with their expected values. The fast convergence of the algorithm suggests the possibility of integrating Kalman filters into an efficient stand-alone detection software with good noise tolerance.

3. Iterative KF-EKF algorithm

As described in Table 2.2, the two sets of unknowns, $\bar{m}(t)$ and $(\bar{r}', \theta, \phi)$, are estimated iteratively and sequentially:

1. *Iteratively:* The KF and EKF algorithms estimate independent variables that serve as input to each other (KF estimates $\bar{m}(t)$ then $\bar{\bar{\beta}}(t)$ which is an input to EKF, EKF estimates $(\bar{r}', \theta, \phi)$ which is an input to KF). The two algorithms are iteratively applied to eventually yield converged values of both unknowns. The sequence used to iterate between KF and EKF is the sequence of transmitter positions throughout the data acquisition process: as the MPV-II is waved atop a target (see Section 3) or as the MetalMapper is driven along a lane (see Section 4). In Table 2.2, the iterative scheme corresponds to sweeping the sensor position $\bar{r}_{\mathrm{Tx}}$ and computing steps (1) and (2).

2. *Sequentially* (index k in Eqs. (2.5) and Eqs. (2.6)): Each individual algorithm updates the value of the unknowns by sequentially processing the data as they become available.

- Initial guess for $\bar{r}', \theta, \phi, \bar{\bar{\beta}}(t)$
- Sweep transmitter positions $\bar{r}_{\mathrm{Tx}}$
  (1) KF: estimate $\bar{\bar{\beta}}(t)$
    · Compute primary field at $\bar{r}'$
    · Compute $\bar{m}(t)$ using Eq. (1.2a)
    · Sweep receiver positions
      Update $\bar{m}(t)$ using Eqs. (2.5)
    End
    · Compute $\bar{\bar{\beta}}(t)$ using Eq. (2.9)
  (2) EKF: estimate $(\bar{r}', \theta, \phi)$
    · Sweep receiver positions $\bar{r}_{\mathrm{Rx}}$
      Sweep time channels
        Update $(\bar{r}', \theta, \phi)$ using Eqs. (2.6)
      End
    End
- End

Table 2.2: KF-EKF iterative algorithm for the estimation of UXO position $\bar{r}'$, orientation (θ, ϕ), and time dependent diagonal polarizability tensor $\bar{\bar{\beta}}(t)$.

(a) KF: the dipole moment $\bar{m}(t)$ is estimated by sweeping all receivers sequentially (at a given $\bar{r}_{\mathrm{Tx}}$ position). The estimation is performed at each time channel, from which the time-dependent polarizabilities are obtained by rewriting Eq. (1.2a) as:

$$\bar{\bar{R}}(\theta, \phi) \cdot \bar{m}(t) = \bar{\bar{\beta}}(t) \cdot \bar{\bar{R}}(\theta, \phi) \cdot \bar{H}^{pr}. \tag{2.9}$$

(b) EKF: since $(\bar{r}', \theta, \phi)$ are supposed time independent, the sequential information to update these parameters is constituted by the sequence of receivers and the sequence of time channels. Hence, a larger dataset is available to estimate the nonlinear parameter, which is a desirable feature.

The sequential processing in the algorithm of Table 2.2 corresponds to the application of Eqs. (2.5) at every time channel by sweeping the sensor positions $\bar{r}_{\mathrm{Rx}}$, and Eqs. (2.6) by sweeping both time channels and sensor positions $\bar{r}_{\mathrm{Rx}}$.

In the subsequent two chapters, the algorithm of Table 2.2 is validated on data collected by the MPV-II and the MetalMapper sensors. In the first case, we consider both static and dynamic data collected on a grid over a well-controlled target. In the second case, dynamic data are processed from large geographical area collections at Camps San Luis Obispo (CA) and Butner (NC).

3. Validation with the MPV-II sensor

1. The sensor

The MPV-II (Man Portable Vectorial sensor II) is a state of the art EMI sensor for the detection and classification of UXO, bringing important flexibility and accuracy improvements compared to the first generation of sensors such as the EM-63 [Ware 03] for example. Some of the key features of the MPV-II include its updated electronics and its vectorial receivers that capture the three components of the secondary magnetic fields. In addition, the MPV-II is compact and lightweight as shown in Figure 3.1, meant to be operated in a hand-held mode by a single operator. The unique horizontal transmit coil, of diameter 49.68 cm, illuminates a small region and needs to be waved atop an area, either randomly or over a pre-defined grid, to collect a sufficiently large amount of data for UXO detection and classification.

The MPV-II can be operated in two modes, referred to as static (or cued interrogation) and dynamic. In this report, we focus on the dynamic mode, meant for rapid land survey: the data collection window is limited to 2.7 ms instead of the usual 25 ms in cued interrogation mode. Target classification is therefore practically excuded and the sensor is mostly used for detection and target volume estimation. In addition, we consider the MPV-II to be waved atop a limit spatial region of about 0.25 m^2, thus presumably looking for a single target only. This is in contrast with the large survey operation mode of the MetalMapper discussed subsequently where targets would come and go as the sensor is driven along a 60 m long lane.

In terms of modelling, the MPV-II is very similar to the first generation MPV: circular transmit loop and cubic vectorial receivers. The main differences in configuration are the physical locations of the receivers and the number and positions of the loops [Fernández 11], which are all differences straightforward to account for in modeling. Consequently, we do not repeat here the formulae implemented to compute the primary field and its derivative, but instead refer the reader to [Grzegorczyk 11].

2. Dynamic mode

There are several differences between a dynamic and a static mode, one of them being the reduced number of averaging cycles used during dynamic data collection compared to a static data collection. As a result, the signal to noise ratio (SNR) is typically degraded in dynamic data, resulting in non-smooth field decay curves. This phenomenon is illustrated in Figure 3.2 across all five receivers and all three field components. The figure shows the field values measured at various cycles, along with their averaged values (black overlapping lines). It is seen for example that receiver 1 essentially measures only noise and that in general the H_x components is more noisy than the H_y or H_z component (for this specific example). The data input to our KF-EKF

(a) Overview of the sensor.

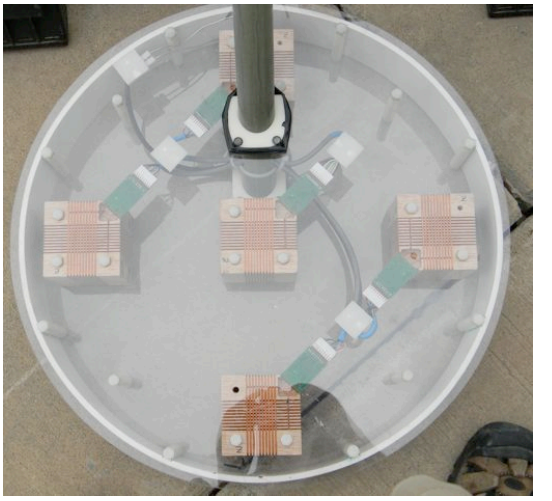

(b) Zoom on sensor head.

Figure 3.1: Photographs of the MPV-II sensor, comprising a boom for hand-held maneuverability at the end of which is located the EMI head. The latter is composed of a circular transmitter (49.68 cm diameter) and five equi-spaced cubic receivers (8 cm side).

algorithm consisted of the averaged field values as shown by the black curves: typically smoother than the curves at each individual cycle, but more noisy than a measurement from a static data collection.

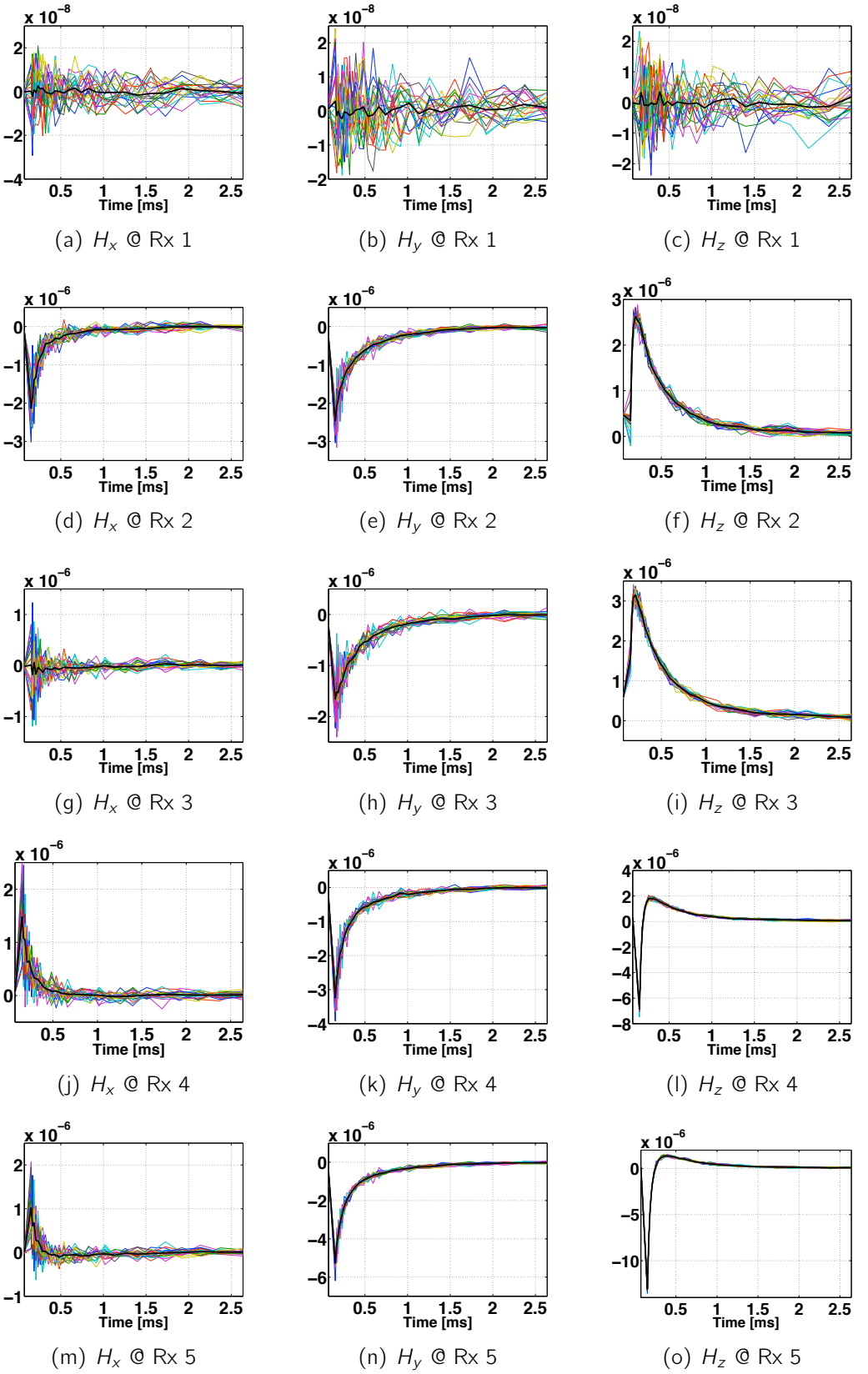

(a) H_x @ Rx 1 (b) H_y @ Rx 1 (c) H_z @ Rx 1

(d) H_x @ Rx 2 (e) H_y @ Rx 2 (f) H_z @ Rx 2

(g) H_x @ Rx 3 (h) H_y @ Rx 3 (i) H_z @ Rx 3

(j) H_x @ Rx 4 (k) H_y @ Rx 4 (l) H_z @ Rx 4

(m) H_x @ Rx 5 (n) H_y @ Rx 5 (o) H_z @ Rx 5

Figure 3.2: Field values and their average (solid black line) from a series of dynamic measurements centered over a 20 mm target.

3. Results

Reference measurement data were available for three targets: a 60-mm, a 57-mm, and a 20-mm, all shown in the insets of Figure 3.3. These datasets were acquired in static mode and are subsequently used to simulate dynamic data with two caveats. First, data include the entire 25 ms window of magnetic field decay: we manually truncate the dataset to the first 2.7 ms. Second, more measurement cycles are used to average the magnetic fields in a static mode (typically 57 cycles of 100 ms) than in a dynamic mode (as few as 10 to 25 cycles are used), resulting in a higher signal-to-noise ratio (SNR) at the expense of a slower data acquisition rate. In order to illustrate the effects of a lower SNR on inversion results, we later analyze a dataset collected in a real dynamic mode. For this first step, however, we resort to the truncated static data collected by all vectorial receivers, at sensor positions spanning a nine-point square grid with 20 cm point-to-point separation. In all cases the targets were located under the central grid point and measurements were started at the top-left grid point. The polarizability curves of Figure 3.3 were obtained by iterating the KF and EKF algorithms (colored circles in the figures) as shown in Table 2.2 where $\bar{r}_{\mathrm{Tx}}$ sweeps the nine-point grid, $\bar{r}_{\mathrm{Rx}}$ sweeps the five receivers, and the time channels span the 25 ms of data collection. The reference curves, in gray in the figures, correspond to polarizabilities obtained with our Gauss-Newton reference algorithm [Grzegorczyk 11] and show the good agreement between the two methods. The 2.7 ms limit is indicated for information purpose, illustrating the fact that most of the decay information is included at later times, unavailable in dynamic datasets. Consequently, dynamic data are mostly used for detection and volume estimation purposes, whereas classification must be done by returning to the target location and operating in cued interrogation mode in order to invert and analyze the entire time decay of the polarizabilities. In the next examples, the datasets of Figure 3.3 are truncated to the first 2.7 ms and are used as input to the KF-EKF algorithm in order to simulate a dynamic operation.

We first study the position convergence capability of the algorithm as function of initial guess $(\bar{r}', \theta, \phi, \bar{\bar{\beta}}(t))$ of Table 2.2. In all cases, the angles are started at zero, the polarizabilities are set to be equal along the three axes with a $1/t$ slope (where t denotes time) starting from an arbitrary value of one at the first time channel, and $\bar{r}'$ randomly samples a surface area between ± 1 m in the (xy) plane, and set to a constant -40 cm in depth, with targets ground truth position at about $(20, -20, -30)$ cm as indicated by the green circles in Figure 3.4. The algorithm is iterated across the nine-point grid for the transmitter positions, across the five receivers each measuring three components of the magnetic field, and across 30 time gates between about 150 μs and 2.7 ms. The noise covariance matrices are set to $\bar{\bar{Q}}_{k-1} = \bar{\bar{R}}_k = \bar{\bar{I}} \times 10^{-20}$ while $\bar{\bar{P}}_k = \bar{\bar{I}} \times 10^{-1}$ since we assume no *a priori* knowledge of true target position and therefore possibly a bad initial guess. The final position estimates, indicated by the blue crosses, all end up within 5 cm of the ground truth (red square) and therefore indicate a good convergence of the algorithm with the available quasi-dynamic dataset. By rerunning the entire KF-EKF algorithm with initial guesses between ± 50 cm, the converged values end up within 2.5 cm of the ground truth, as illustrated in Figure 3.5 (with similar convergence bounds on the depth, not shown here). These accurate and consistent position estimates reveal that the 2.7 ms time window of data collection is sufficient to properly estimate the location of all the three targets under investigation, including that of the small 20-mm item.

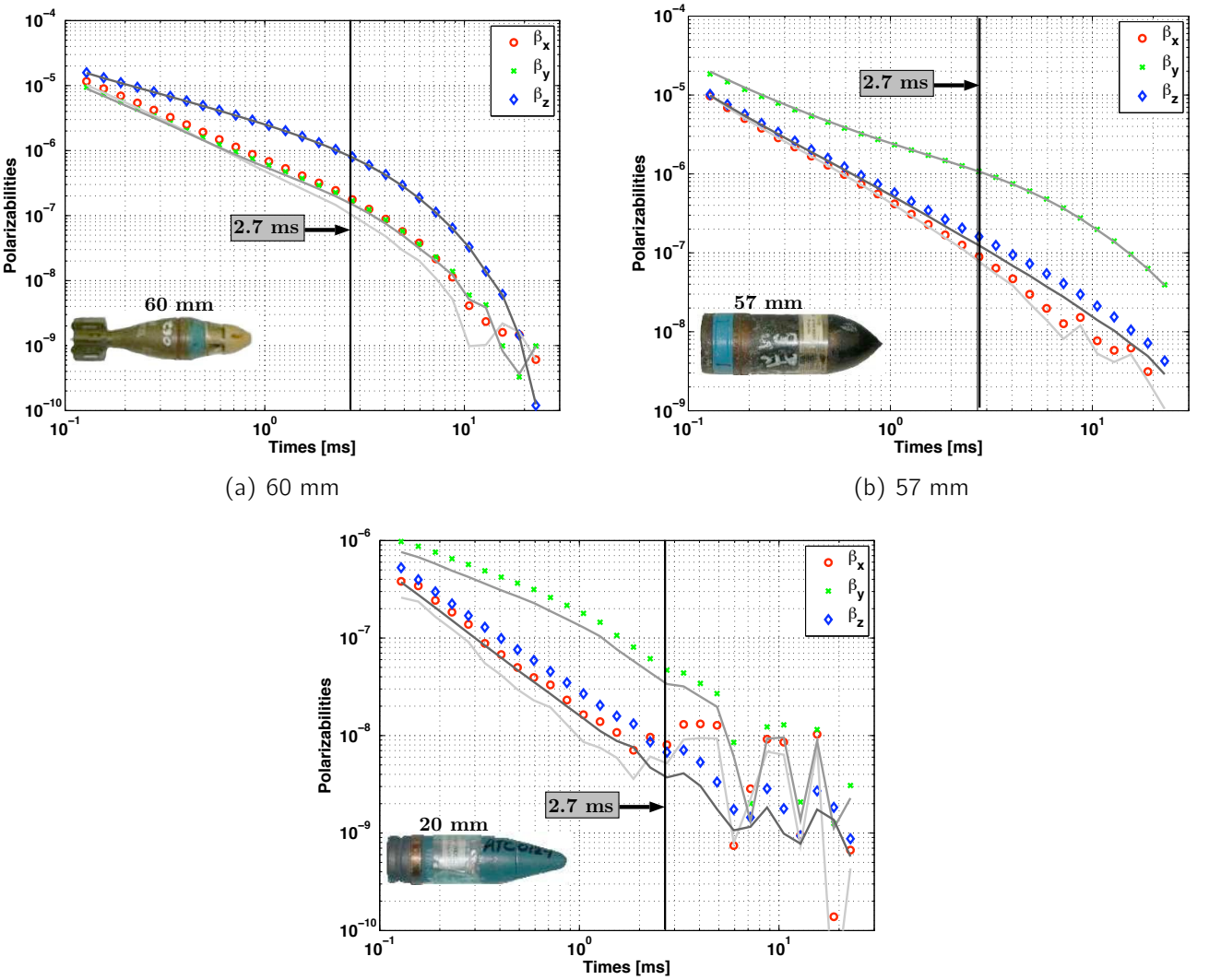

(a) 60 mm

(b) 57 mm

(c) 20 mm

Figure 3.3: Polarizability of three UXO (see insets) from static data measured by the MPV-II. The 2.7 ms limit of dynamic data collection is indicated. The reference gray signatures are based on a Gauss-Newton inversion [Grzegorczyk 11].

Next we consider an actual dynamic dataset collected atop the small 20-mm UXO. Compared to the truncated static dataset of the previous example, the signal-to-noise ratio of dynamic measurements is deteriorated owing to the fewer cycles used to average the data. A comparison of measured field values in static and dynamic mode is presented in Figure 3.6. The configuration is that of an offset target compared to the MPV-II as shown in Figure 3.6(a), with the target along the $\hat{y}$ direction. Field plots at the closest three receivers illustrate the smoother nature of the static dataset in all three components of the measured field. In particular, the noise in the H_z component (usually dominant) has an important influence on the inversion results and algorithm convergence.

The KF-EKF algorithm is run in a similar way as in the previous example, in particular with the same initial values of the covariance matrices $\bar{\bar{Q}}_{k-1}$, $\bar{\bar{R}}_k$, and $\bar{\bar{P}}_k$. Since the algorithm is se-

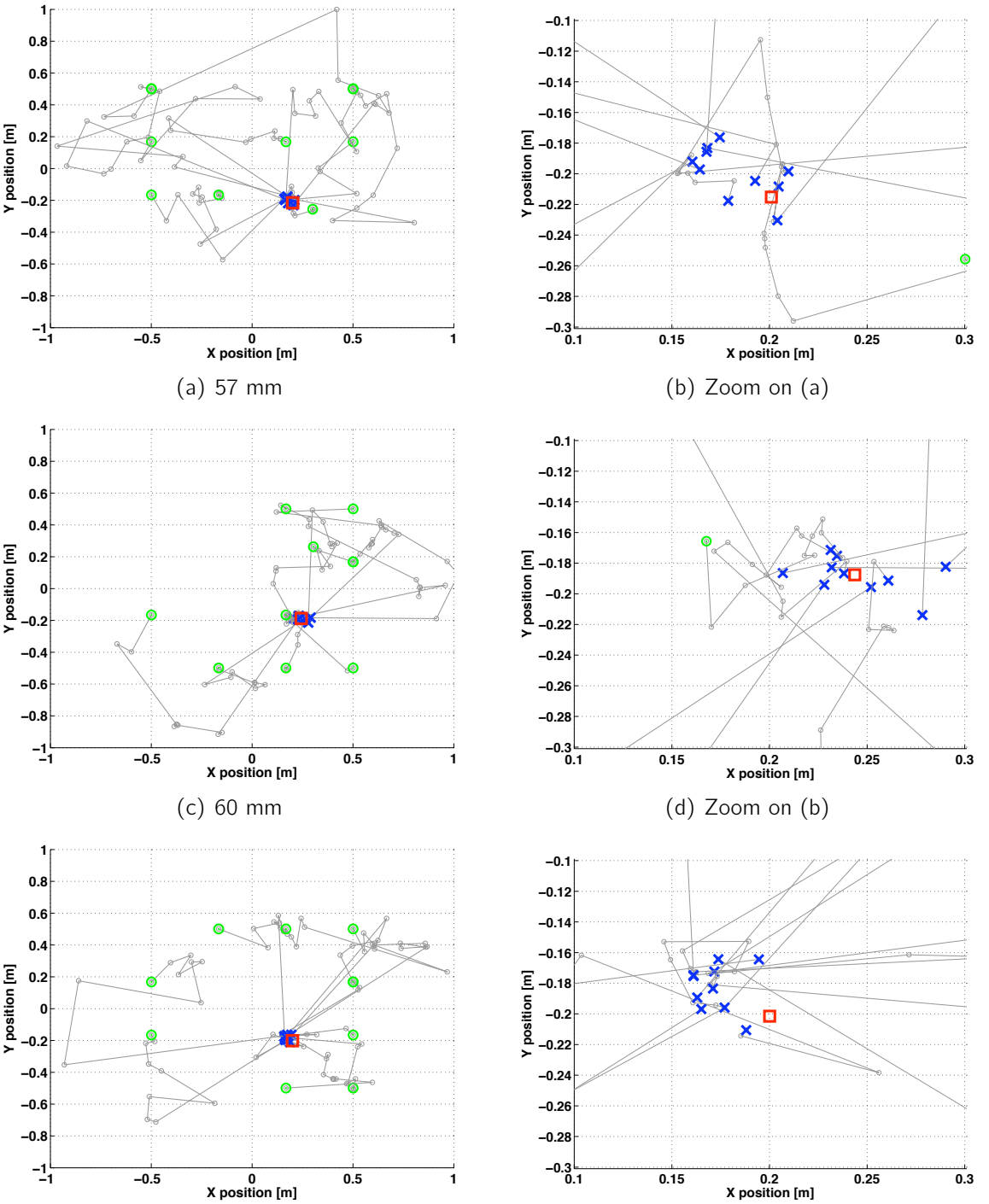

(a) 57 mm (b) Zoom on (a)

(c) 60 mm (d) Zoom on (b)

(e) 20 mm (f) Zoom on (c)

Figure 3.4: Evolution of position estimates in the (xy) plane as the filter is updated for various transmitter positions. The random initial guesses, between -1 m and $+1$ m in the (xy) plane, are indicated by the green circles and the final estimated positions are indicated by the blue crosses. The ground truths are indicated by red squares. The gray paths illustrate the sequential estimates during the iterative process.

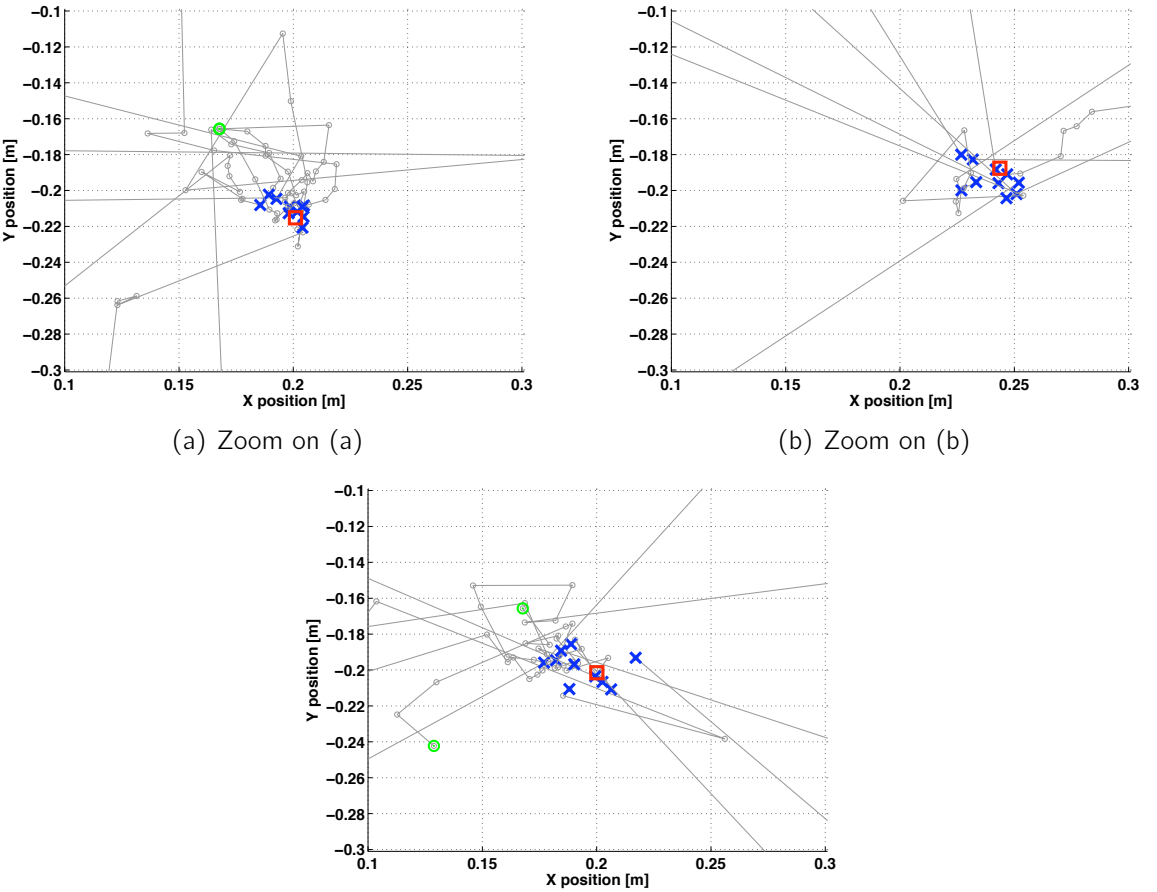

(a) Zoom on (a)

(b) Zoom on (b)

(c) Zoom on (c)

Figure 3.5: Same as Figure 3.4 with initial guesses between −0.5 m and +0.5 m.

quential, however, it is possible that one noisy measurement at a given instance k destabilizes the solution and yields a divergence (such phenomenon is less likely to happen with a non-sequential algorithm where all the data are processed simultaneously, thus minimizing the influence of one bad measurement). In order to prevent such divergence from happening, we implement a memory scheme whereby the newly estimated parameters $(\bar{r}'_k, \theta_k, \phi_k, \bar{m}_k(t))$ are retained only if they yield a lower field mismatch than the previous estimates $(\bar{r}'_{k-1}, \theta_{k-1}, \phi_{k-1}, \bar{m}_{k-1}(t))$. If not, the $(k-1)$ parameters are propagated to instance k and the KF-EKF algorithm is iterated to the $(k+1)$ instance. The polarizabilities resulting from this updated/select scheme for the 20-mm UXO are shown in Figure 3.7 inverted at a position $(-3, -3, -40)$ cm along the $\hat{y}$ direction. This represents a difference of 3 cm and 2 cm in the $\hat{x}$ and $\hat{y}$ directions, respectively, and a similar depth to the inverted position using the truncated synthetic data (UXO inverted at $(0, -1, -40)$ cm). The main polarizability in Figure 3.7 follows the expected decay and amplitude properly but the two weaker ones are considerably more noisy, which we attribute to the lower SNR as discussed above. Nonetheless, this example illustrates the possibility of using the MPV-II sensor for the dynamic detection of targets as small as the 20-mm.

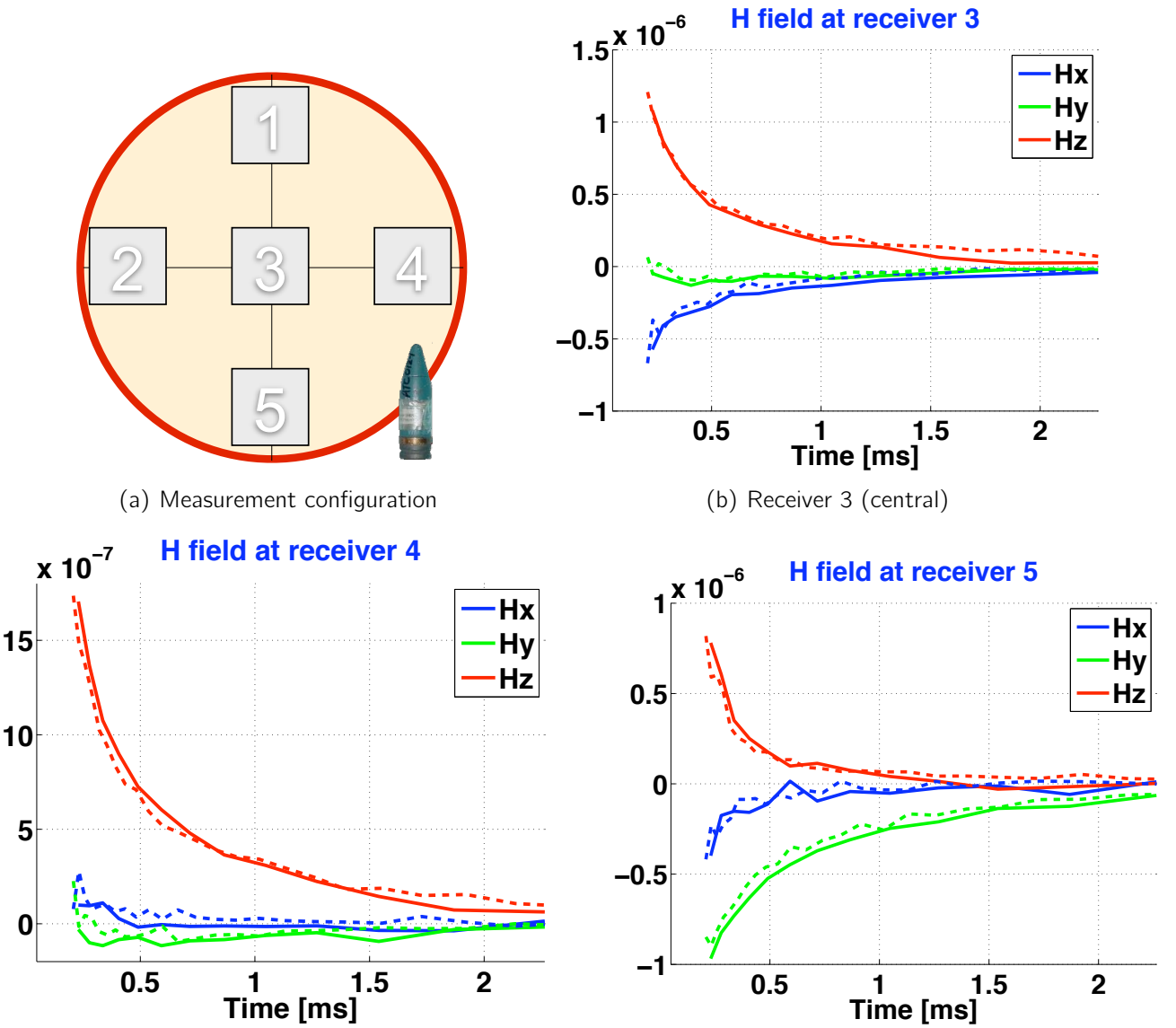

(a) Measurement configuration

(b) Receiver 3 (central)

(c) Receiver 4

(d) Receiver 5

Figure 3.6: Comparison between field components collected atop an off-centered 20-mm UXO in a static mode (solid lines) truncated at 2.7 ms and a dynamic mode (dashed lines).

4. An alternative formulation

The purpose of the algorithm presented so far is to invert for $\bar{r}$ and β in Eq. (1.1)-(1.2), which is an approach adopted by the vast majority of researchers working with the dipole model. Within the KF-EKF algorithm developed here, β are inverted using a KF approach (linear part of the model) while $\bar{r}$ is inverted using an EKF approach (non-linear part). In general, the EKF algorithm does not guarantee convergence and its efficacy usually depends on how strongly nonlinear the problem is. In order to ensure a better convergence of the EKF algorithm, it is possible to reduce the nonlinearity of the problem by inverting for modified variables.

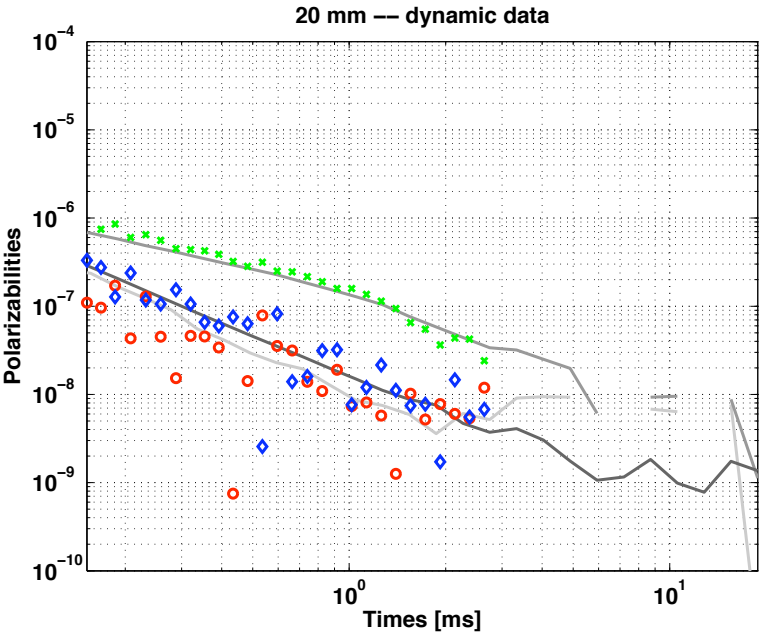

Figure 3.7: Polarizabilities of a 20-mm UXO obtained from dynamic MPV-II measurements. The reference gray signatures are based on a Gauss-Newton inversion [Grzegorczyk 11].

The formulation starts by writing $\bar{r}$ as

$$\bar{r} = \hat{r}\, r \;= \bar{r}_{\mathrm{Tx}} + \bar{r}_{\mathrm{Rx}} - \bar{r}' \tag{3.1a}$$

$$\text{where} \qquad \hat{r} = \;\hat{x}\sin\theta\cos\phi + \hat{y}\sin\theta\sin\phi + \hat{z}\cos\theta \tag{3.1b}$$

where $\bar{r}$ is the same distance vector as in Eqs. (1.1).

In general, the angles (θ,ϕ) are not good parameters to invert for since they depend on both the transmitter $\bar{r}_{\mathrm{Tx}}$ and receiver $\bar{r}_{\mathrm{Rx}}$ positions (in addition to depending on the position of the UXO $\bar{r}'$). Hence, an inversion algorithm that collectively uses all data (from all Tx and all Rx) gains little by adopting (θ,ϕ) as unknowns since the latter vary at each data point. The situation is very different for a *sequential* estimation algorithm such as the KF-EKF algorithm: (θ,ϕ) can be adjusted by the known quantities $\bar{r}_{\mathrm{Tx}}$ and $\bar{r}_{\mathrm{Rx}}$ at every iteration of the algorithm, leaving only local angles to be inverted for in order to estimate $\bar{r}'$. The non-linearity of the magnetic field with respect the unknowns (θ,ϕ) is much reduced compared to the non-linearity with respect to $\bar{r}$.

The angles (θ,ϕ) provide information on the *direction* at which the UXO is located, and the remaining parameter $1/r^3$ provides the range information, i.e. how far in the given direction is the UXO. Here again, in order to limit the nonlinearity of the magnetic field with the unknown, we solve for $1/r^3$ instead of solving for r itself, contributing to more stability of the EKF algorithm. We also note that the dyad $\hat{r}\hat{r}$ as well as its derivative with respect to θ and ϕ are all straightforward to compute.

Consequently, we can reformulate the algorithm to solve for $(\theta,\phi,\, 1/r^3)$ and process the data using the EKF approach. The polarizabilities, remaining linear, are still obtained from the KF approach.

An example of inversion is presented in Figure 3.8, comparing the predictions between the

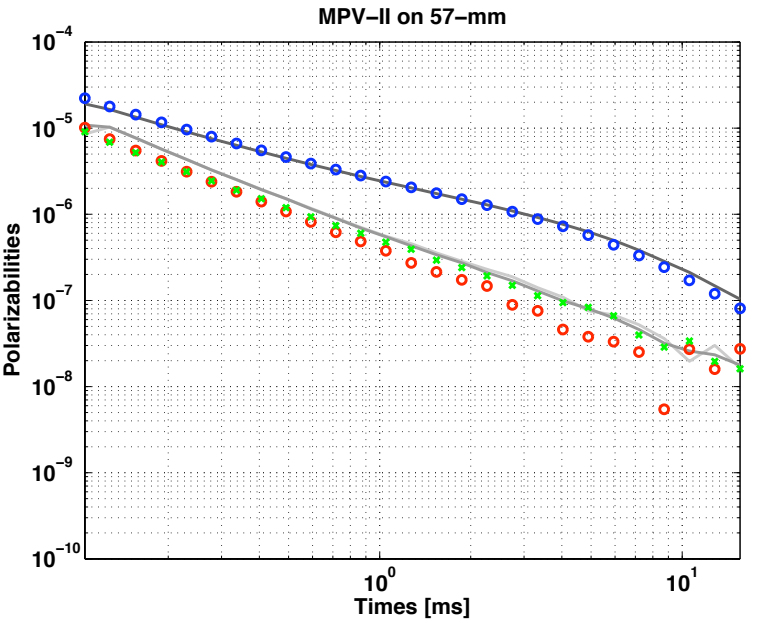

Figure 3.8: Polarizabilities obtained by an iterative KF-EKF sequential algorithm from MPV-II data collected over a 57-mm UXO. The reference gray signatures are based on a Gauss-Newton inversion [Grzegorczyk 11]. The inverted positions are $(4, -5, -42)$ cm and $(0, -3, -41)$ cm obtained with the KF-EKF and GN algorithms, respectively, whereas the ground truth is listed as $(0, 0, -35)$ cm to the tip of the vertical-nose-up 57-mm.

KF-EKF algorithm and our Gauss-Newton reference, from data collected over a 57-mm UXO. The robustness of the results to initial guess and noise levels (not shown here) confirms the improved stability of the modified algorithm and proposes it as a possible alternative formulation to investigate in the future.

4. Validation with the MetalMapper sensor

1. The sensor

The MetalMapper is also considered a next generation sensor like the MPV-II. Among its unique features are three large perpendicular transmit coils (1 m $\times$ 1 m) with electronically switched TEM transmitter loop drivers that provide illumination diversity of the targets from a single sensor position, and seven fully vectorial receivers similar to those of the MPV-II. Additional hardware and operational information can be found in [Prouty 11]. A photograph and a schematic representation of the receiver locations are shown in Figure 4.1: the two perpendicular vertical transmitter coils are clearly visible whereas the horizontal transmitter is enclosed in a wooden casing along with the receivers (hence invisible). Like the MPV-II, the MetalMapper can be operated in either a static – or cued interrogation – mode whereby full data sets are collected atop previously flagged locations and used for classification purposes, or in a dynamic – or target mapping – mode, whereby data are acquired at a fast rate while the sensor is moving. In 2009 and 2010 the sensor participated in live site demonstrations at the former Camp San Luis Obispo California (SLO) and the former Camp Butner, North Carolina, in order to validate both operation mode in realistic field situations. In a cued interrogation setting, the three transmit coils fire sequentially to excite independent eddy currents in the subsurface targets, and the secondary magnetic field components (H_x, H_y, H_z) are collected by the seven receivers over a decay period of about 25 ms. The dataset is therefore composed of 63 time decay magnetic field curves (three transmitters, seven receivers, three components) which need to be processed and converted into position and time-dependent intrinsic polarizabilities of targets. Various field tests have shown that the dataset collected by the MetalMapper is compatible with real field detection and classification of various UXO [Prouty 09b, Prouty 09a].

In this report, however, we are interested in the dynamic mode, meant for rapid land surveys and for the creation of target maps to which operators can return if necessary. The main feature of a dynamic operation is therefore speed. At the data acquisition stage, it is achieved by (1) using only the horizontal transmit coil (hence one transmitter instead of three), and (2) limiting the recording time to the first 2.7 ms of field decay (instead of the traditional 25 ms) and using less averaging windows, thus resulting in lower signal to noise ratios than in cued interrogation mode.

The protocol at the two demonstration sites mentioned above was to drive the MetalMapper along lanes separated by about 0.75 m and acquire data points at 100 ms intervals, thus creating magnetic field maps of the area to be surveyed. Tracking of the sensor positions was performed through an on-board RTK GPS (real-time kinematic global positioning system), providing a accuracy of about 2 cm in latitude and longitude directions. The conversion into Northing and Easting coordinates necessary for our algorithm was performed following [Hager 89, Smith 90].

The attitude of the sensor platform was obtained through a two-axis accelerometer to measure pitch and roll angles, and a three-axis magnetometer to measure heading angle with reference to the true magnetic north [Prouty 11]. This information is necessary in order to properly rotate the magnetic field components so as to produce an estimated position in a global reference frame (arbitrarily chosen).

Inherent to purpose of land survey where target location is unknown, every dynamic shot is used semi-independently, i.e. data corresponding to successive sensor positions are not combined into a single dataset but are used independently. However, the estimated parameters from one sensor position are used as input at the next position. If the dominant signal between two consecutive sensor positions correspond to the same target, the initial guess is good and helps the filter converge more rapidly. If not (for example when a target is being lost because too far from the sensor already, or when a second target produces a stronger signal), the filter needs to adjust the estimated parameters from the inaccurate initial guess to the new solution. The data processing follows that of Table 2.2 exactly where the outermost loop (sweeping $\bar{r}_{\mathrm{Tx}}$) corresponds to the sequence of transmitter positions along each lane.

2. Results from KF-EKF

We first consider the dynamic data collected at Camp Butner. The area surveyed is approximately five meters by 60 meters, sampled into eight lanes separated by about 75 cm and indicated as thin black lines in Figure 4.2. The background in the figure corresponds to the interpolated z-component of the magnetic field at the central receiver, plotted on a logarithmic scale. It can be seen that the map contains many peaks, typical of a soil highly contaminated with clutter items. A series of seeded items are placed along a line at an Easting relative coordinate of about 2.5 m. Referring to the figure, the items are (from bottom to top) a shotput, a 37-mm projectile, three small ISO, a shotput, and a pit, all identified by red circles.

The selection of targets from inversion results is currently performed on a per-lane basis and in two stages. First the KF-EKF algorithm processes every data point semi-independently to produce an estimated target position and signature, regardless of the fact whether there is a target or not. Second, the estimated positions are post-filtered to identify those detection results that correspond to actual targets based on result consistency in Northing, Easting, and depth inversions. This process is best illustrated with an example, for which we refer to Figure 4.3. The figure shows the sequence of positions estimated by the KF-EKF algorithm when the MetalMapper is driven along lane 5, at relative Northing coordinates between 30 m and 32.5 m, where x refers to Easting, y to Northing, and z to depth. In the absence of target, the inverted (x, y, z) coordinate appear random from one sensor position to the next, not exhibiting any consistency or relation to one another, allowing the post-processing algorithm to filter these positions out. In the presence of a target, however, the inverted (x, y, z) coordinates exhibit a pattern easily identifiable. In the example of Figure 4.3, the strongest signal is produced by the last shotput located at a relative Northing coordinate of about 31.5 m. The inverted y coordinate corresponds to the target position along the driving direction of the sensor: the target is first *in front* of the sensor (positive y), then at the same Northing level as the sensor (y close to zero), then *behind* the sensor (negative y). At 30.5 m, the target is still too far away from the sensor to produce a stable inversion and the coordinates are seen to be quickly varying, indicating no convergence.

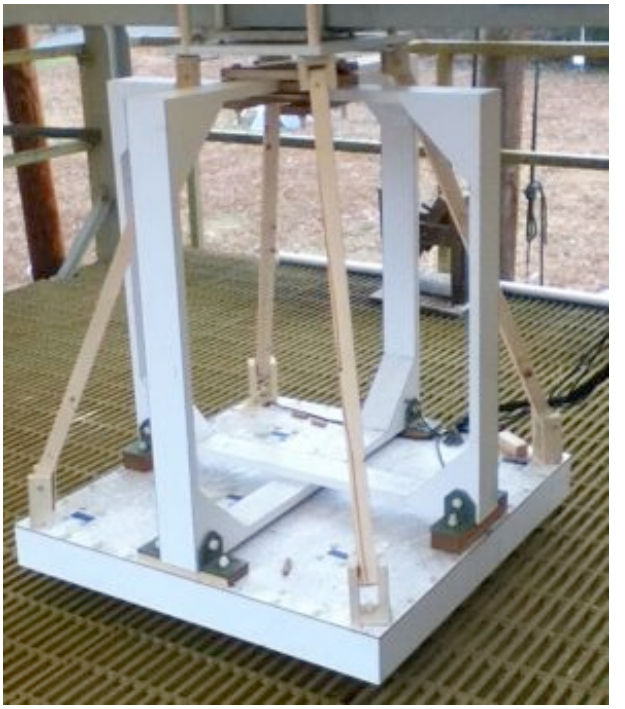

(a) MetalMapper sensor.

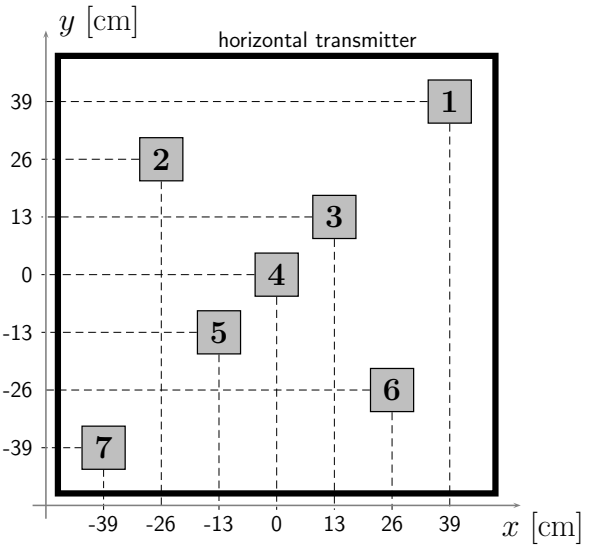

(b) Receivers and $\hat{z}$ oriented coil.

Figure 4.1: Geometry of the MetalMapper used in the algorithm. The primary field coil dimensions are 1 m × 1 m and produce a magnetic field computed from the addition of four wires supporting the same constant current. For computational efficiency, the received field is computed at the center of each receiver only, i.e. the finite size of the receiving cubes is not accounted for.

Between about 31 m and 32 m, the inverted y position is seen to follow the dashed black line which corresponds to the local y position of the sensor (with arbitrary center): a good match

indicates a stationary target, as expected. Within this range, the inverted Easting and depth present variations due to the noisy data, yet the amplitudes of these variations are smaller than when the algorithm does not converge, indicating a consistent Easting position and a constant depth, again corroborating the detection of a stationary target. Consequently, inversion results are either discarded (around 32.5 m for example, we conclude that no target is detected) or flagged as targets of interest based on the pattern in (x, y, z) evolution with the sensor motion.

Applied to Camp Butner data, this process produces the estimated positions marked by white crosses in Figure 4.2 which are seen to usually overlap well with the magnetic field peaks. In some cases, however, the overlap appears to be poor, for two reasons. First, not all the lanes pass close to the seeded items: some are far enough to measure a very weak field and yet close enough for this field to be dominant and to drive the inversion algorithm. In these cases, the algorithm tries to detect the target despite the weak measured fields, resulting in inaccurate estimates. For example we have confirmed that the first shotput (relative Easting about 2.75 m, relative Northing about 7 m) is properly located when the MetalMapper travels along lanes four and five from the left, adjacent to the target, but that the predictions are worst along lanes three and six. The associated predictions correspond to the series of picks between 3 m and 4 m in relative Easting, away from the red marker. Hence, lane 6 for example is too far from the actual target to detect it accurately and given the noisy data and weak fields, the predictions are the best the algorithm could achieve. The second reason for possible mismatch between the white crosses and the field peaks in Figure 4.2 is that the picks are not post-processed in the figure and not averaged, but are presented as raw results. We again refer to Figure 4.3 to illustrate this concept: once such a pattern in inverted (x, y, z) has been identified, we select a window of detection, where the target is believed to be properly picked. In this case, such window could be defined between 31 m and 32 m. Un-filtered results would then plot all the picks within this window, yielding all the white arrows in Figure 4.2. A post-processing of these data could limit the number of picks to the point where $y = 0$ (at about 31.5 m in this example), or average all the picks within 31 m and 32 m, both of which would produce a single white pick. Such procedure is adopted in the next example. By showing unprocessed picks here, however, we confirm that the algorithm does consistently converge to reasonable estimates for all positions that are close to a given target, thus confirming that a target can be flagged without having to be right under the sensor. This implies that the MetalMapper can command a vehicle to stop while still ahead of a target, which can be an important safety feature in real field operations.

The second example pertains to a similar situation with data collected at former Camp San Luis Obispo (SLO), along ten lanes spanning an area of about 7 m by 60 m. Unlike Camp Butner, the subsurface at SLO contains much less clutter items as can be seen by the more uniform background in Figure 4.4 (the background again corresponds to the interpolated H_z value at the central receiver). The dynamic data were post-processed by G&G Sciences Inc. using a method based on matched filter to a sphere response [George 11], thus allowing a direct result comparison with our KF-EKF approach.Results are shown in Figure 4.4 comparing the blue circles (picks by G&G Sciences Inc.) and the red crosses (averaged picks by the present KF-EKF algorithm). Like in the previous example, our target picks are identified by regions where the inverted (x, y, z) positions follow trends as shown in Figure 4.3: a y coordinate matching that of the moving platform, and quasi-constant x and z coordinates. Unlike Figure 4.2, however, the range of values corresponding to a likely target are here averaged to produce a single pick on the

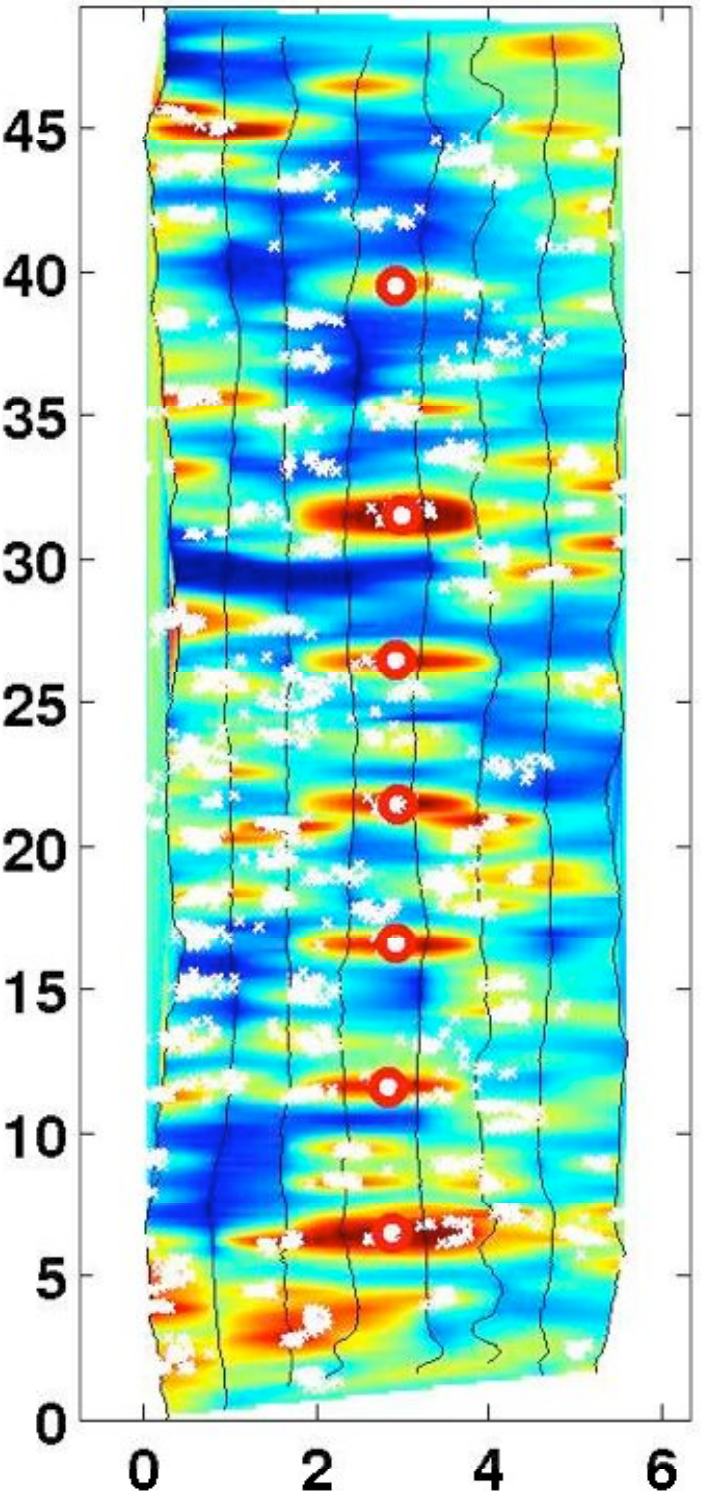

Figure 4.2: Target picks from dynamic data collected at Camp Butner, NC. The background represents the interpolated $\log_{10}$ values of the H_z component at the central receiver. The color scale is chosen to produce red and blue regions at location of strong and weak magnetic field values, respectively.

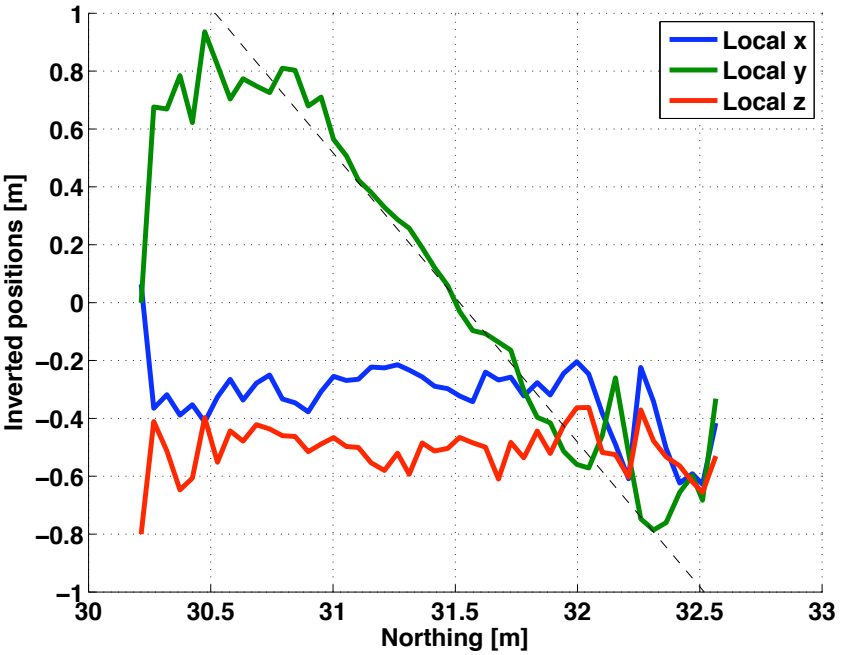

Figure 4.3: Inverted positions around a Northing position of 31.5 m in Figure 4.2.

map, thus resulting in much less red cross in Figure 4.4 than white crosses in Figure 4.2. The matching with results from G&G Sciences Inc. is seen to be overall very good, with target picks from the two methods overlapping each other. Some picks from G&G Sciences Inc., however, are seen to stand alone: when they do not correspond to isolated detection points, we have confirmed that these picks could be matched by our algorithm by relaxing slightly the selection criterion. For example, the second target missed on lane 1 (dashed left-most lane) could have been picked if we had allowed variations in Easting (x coordinate) and depth (z coordinate) of more than 15 cm within the detection window.

A more quantitative comparison between the inverted positions is shown in Table 4.1 where we also compare the KF-EKF predictions with those of our reference Gauss-Newton algorithm [Grzegorczyk 11]. Somewhat expectedly, it is seen that the largest error corresponds to the component in the traveling direction y whereas predictions in Easting and depth are typically within a few centimeters. The larger standard deviations are due to the fact that the entire detection window is used to compile these results, including when the target is outside the physical range of the sensor. Although we have confirmed that targets do not need to to be exactly under the sensor to be detected, these extreme positions typically result in larger errors and produce the standard deviations between 10 cm and 20 cm reported in Table 4.1.

As a further validation, we compare the integrated polarizabilities obtained by G&G Sciences Inc. and by the KF-EKF algorithm. Although a 2.7 ms data collection window is of little use for classification purposes, it can provide first hand volumetric information about the targets that can be used in a dig/no-dig decision making. The metric is the root mean square RMS_β of the time dependent polarizabilities across the N time gates (between times t_1 and t_N) and across the entire M-point detection window (in the case of Figure 4.3 for example, the detection window

	Mean [cm]			Standard deviation [cm]		
	$\lvert dx\rvert$	$\lvert dy\rvert$	$\lvert dz\rvert$	$\lvert dx\rvert$	$\lvert dy\rvert$	$\lvert dz\rvert$
KF-90ms vs. GN	0.5	4.4	1.3	9.6	18.2	6.9
KF-90ms vs. G&G	0.7	14.1	0.6	9.2	15.7	8.7

Table 4.1: Mean and standard deviations (in centimeters) of the positions obtained by (1) the KF-EKF algorithm compared to the Gauss-Newton (GN) reference and (2) the KF-EKF algorithm compared to the results provided by G&G Sciences Inc.. The sample size is of 55 targets over 10 dynamic lanes at Camp San Luis Opbispo, each lane being about 60 m in length.

is defined as between 31 m and 32 m in Northing coordinates) defined as

$$\mathrm{RMS}_\beta = \sqrt{\frac{1}{MN}\sum_{\bar{r}_{\mathrm{Tx}}=\bar{r}_{\mathrm{Tx}_1}}^{\bar{r}_{\mathrm{Tx}_M}}\sum_{t=t_1}^{t_N}\Big(\beta_x(\bar{r}_{\mathrm{Tx}},t)^2+\beta_y(\bar{r}_{\mathrm{Tx}},t)^2+\beta_z(\bar{r}_{\mathrm{Tx}},t)^2\Big)}\,. \tag{4.1}$$

Identifying a one to one correspondence between G&G Sciences Inc. and the KF-EKF target picks allows a one to one comparison between the corresponding normalized RMS_β, as shown in Figure 4.5. Despite magnitude differences of the three larger targets (which is a topic of further investigation requiring additional data collection with ground truth), all the most prominent targets are identically selected.

3. Note on processing time

Compared to the previous task, our purpose was to speed up the algorithm and achieve "real time" computational efficiency. This was motivated by a series of discussions while working with the MetalMapper in a field setting, where the need of a "usable algorithm" was emphasized, i.e. a code that can actually be ported onto a sensor's control panel and used during a data acquisition campaign. We therefore reimplemented our algorithm from scratches, leaving the KF part (Kalman filter) essentially unchanged but drastically optimizing the EKF part (Extended Kalman filter) for position estimation. As a result, our algorithm currently runs in about 250 ms and provides inversion information including, location, depth, polarizabilities (over the short time intervals during which data are collected in a dynamic setting), volume information, and detectability criterion. Various metrics have been tested for the detectability criterion and the one currently retained is based on a linear regression of the inverted polarizabilities in log-log space.

The current time of 250 ms is obtained on a regular 2×2.8 GHz Quad-Core Intel Xeon computer. Although it is likely to be a more powerful computer than the available DAQ currently associated with the MetalMapper, it is also not unrealistic to have such computer power on-board. In addition, we have not performed any hardware acceleration such as using GPU or parallelization. Hence, if necessary, it appears that it would be very possible to achieve a computation time of 100 ms as we had originally targeted, and realistically call our algorithm "real time".

In fact, shorter times can already be achieved: the KF-EKF algorithm runs with typically ten realizations and loops through all time channels. By further reducing these parameters, we can achieve a computational time of about 70 ms (hence below our self-suggested 100 ms limit), yet

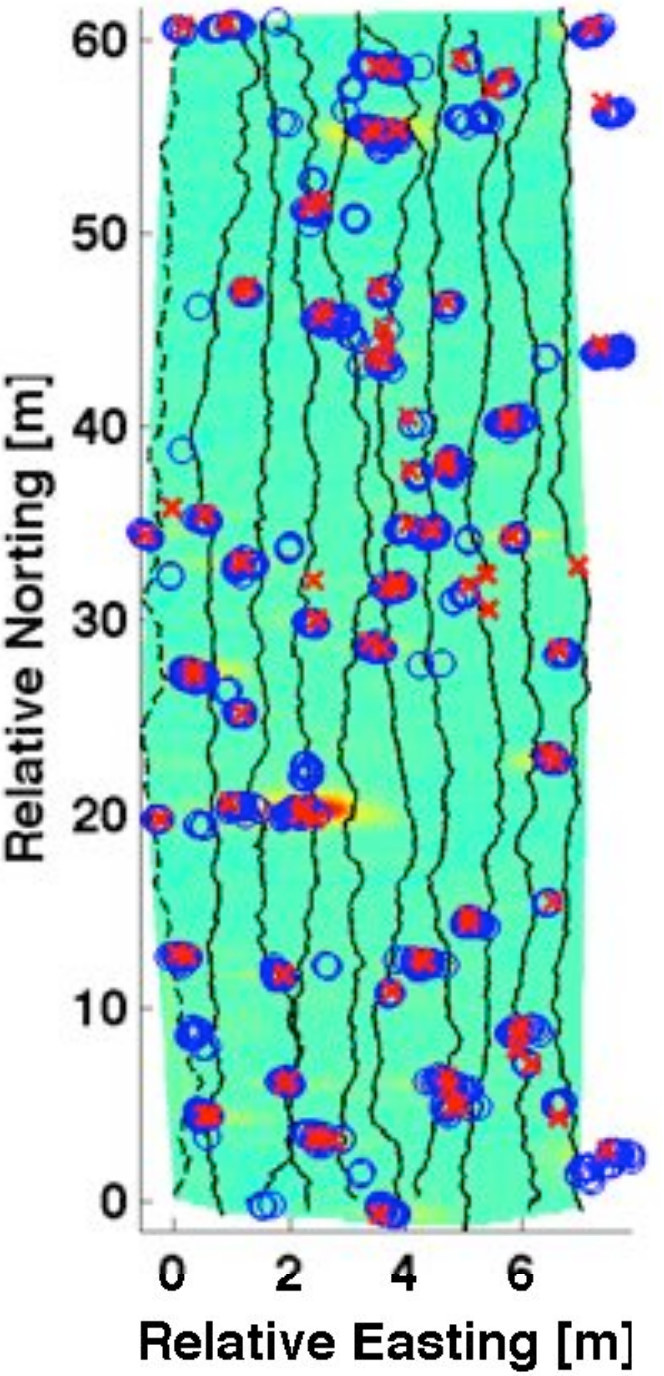

Figure 4.4: Comparison between G&G Sciences Inc.target picks (blue circles) and KF-EKF algorithm target picks (red crosses) for Camp San Luis Obispo dynamic MetalMapper data.

at the expense of result accuracy. The latter is being currently evaluated and preliminary results are shown in Figure 4.6. The figure shows a history of estimated positions as the MetalMapper travels by a target. The three sub-panels correspond to three settings of the algorithms, from many realizations and many iterations yielding a processing time of 850 ms, to fewer realizations and iterations yielding a processing time as low as 70 ms. In all cases the target is properly

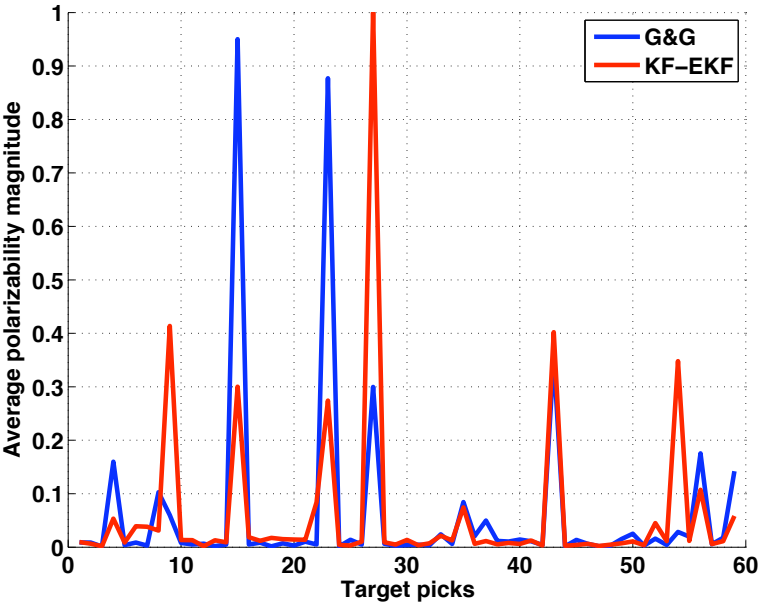

Figure 4.5: Comparison between the averaged polarizabilities obtained by G&G Sciences Inc. (blue line) and by the KF-EKF algorithm (red line) across all target picks.

located and locked on, but with varying degrees of error. A quantitative study will be undertaken to document these errors more specifically.

Finally, we would like to emphasize that the KF-EKF is probably best applied to this precise situation, whereby data are gathered on the fly over targets that need to be locked on for a certain time period (during which the target is visible to the MetalMapper). We put this situation in contrast to waving the MPV in search of a single target: in this case, best results are obtained when all data points are used simultaneously in order to obtain good inversion accuracy. This is the approach we adopt in our Gauss-Newton algorithm. With a driving MetalMapper, however, the problem is really sequential: each shot constitutes a sequential information that can be used to lock onto a target (as it passes by the sensor), or unlock from a target that moved away from the sensor field of view.

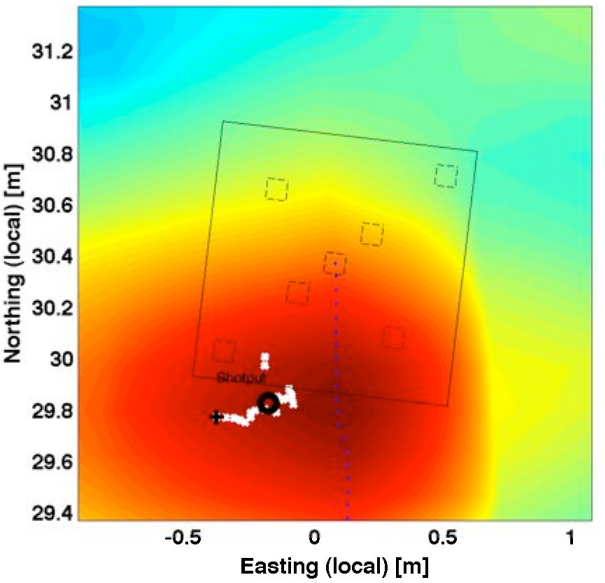

(a) Setup 1: 850 ms processing.

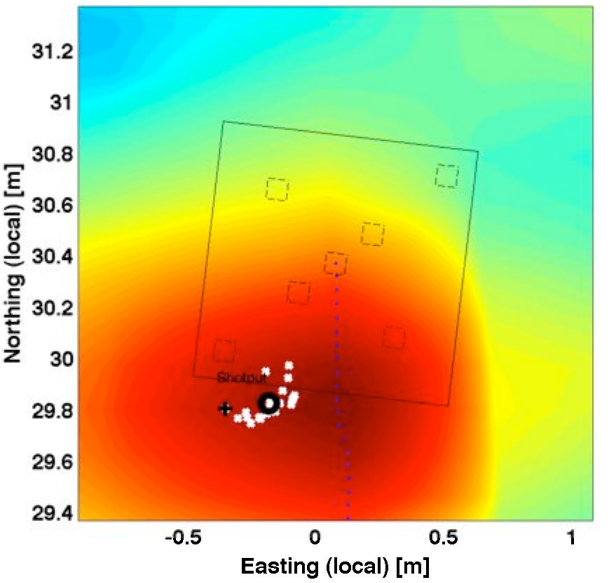

(b) Setup 2: 200 ms processing.

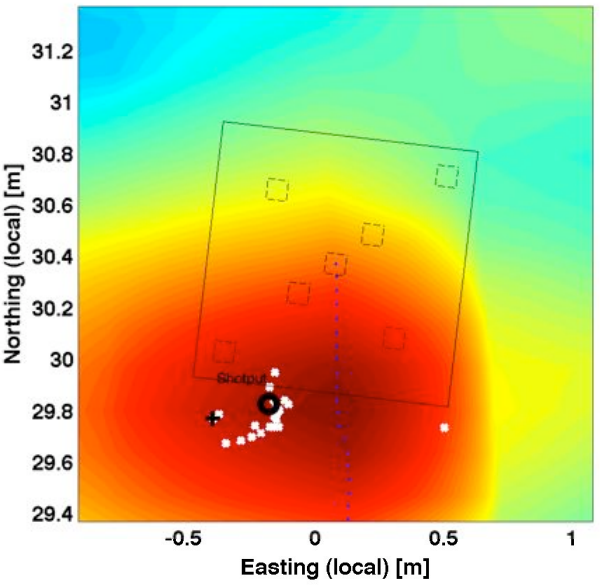

(c) Setup 3: 70 ms processing.

Figure 4.6: Newly implemented KF-EKF algorithm with three different settings, yielding three different data processing times. The figures show a history of estimated positions as the MetalMapper drives by a target.

4. Graphical User Interface proposal

The KF-EKF algorithm is more than just a detection algorithm since it provides an estimate of all the parameters in the dipole model of Eq. (1.1): position, depth, angles, and polarizabilities. Moreover, the inverted parameters themselves can be combined to extrapolate additional information:

(i) Polarizabilities can serve to estimate target volume and three-dimensional aspect ratios,

(ii) Positions and depths can be examined for consistency at sequential sensor positions to inform on whether the target is likely a UXO or not,

(iii) Polarizabilities can be matched to a library to further estimate the probability of UXO,

(iv) Further processing can use $(\bar{r}', \theta, \phi, \bar{\bar{\beta}}(t))$ collaboratively to refine all estimates mentioned above.

The information content is therefore rich and needs to be displayed appropriately if it is to be used by an operator in a real-time fashion. An example of a graphical user interface (GUI) is shown in Figure 4.7 where all the information mentioned above is displayed in real time:

➢ Left column: Position information

- Top: lateral position in the (xy) plane showing the inverted values, a schematic representation of the sensor, and the field background (here interpolated between all receivers)
- Bottom: Depth as function of past sensor positions, which allows to quickly check for consistency (usually associated with a real target as opposed to a clutter item)

➢ Right column: Information from polarizabilities

- Top: aspect ratio in the (xy) and (xz) plane, showing an ellipse with axes $(\beta_x(t_0), \beta_y(t_0))$ and $(\beta_x(t_0), \beta_z(t_0))$ at a certain time t_0.
- Middle: Metric indicating the probability of presence of a target of interest. In this example, the metric corresponds to a correlation of the three polarizabilities to a linear decay within the first 1 ms of data acquisition. A consistently good correlation is usually related to a real target whereas a poor correlation is associated with either clutter items or algorithmic divergences (when no target is actually present beneath the sensor).
- Bottom: Actual inverted polarizabilities $(\beta_x(t), \beta_y(t), \beta_z(t))$ here shown within a 1 ms window.

Figure 4.7 corresponds to a snapshot at a certain position of the MetalMapper during data acquisition at Camp Butner. The full movie was presented along with a summarizing poster at the SERDP Annual Symposium (Nov. 29 – Dec. 1 2011, Washington DC).

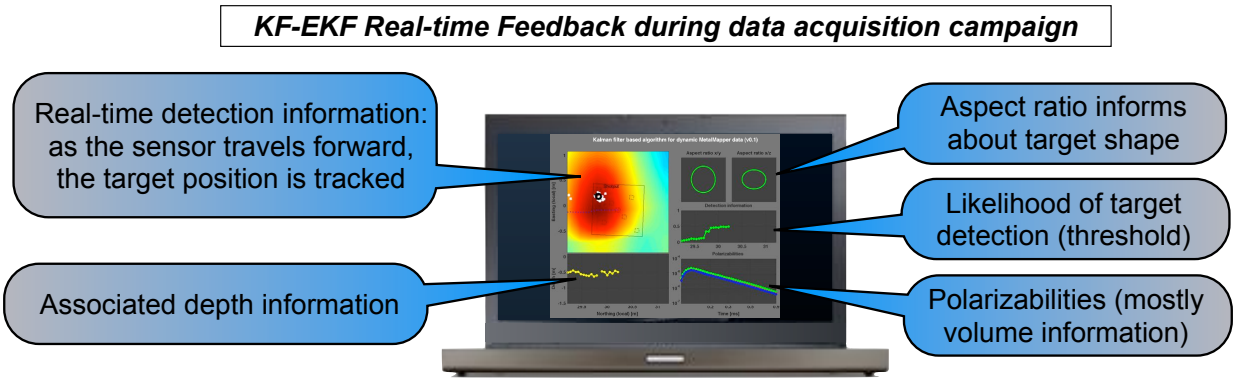

Figure 4.7: Snapshot of the GUI and results obtained from the processing of dynamic lane 33 at Camp Butner. Results are obtained with the KF-EKF algorithm and show the predicted positions in the (xy) plane, the predicted depth, the inverted polarizabilities with a related aspect ratio of the UXO, and a detection metric based on a linear fit of the polarizabilities.

Conclusions and future perspectives

We have demonstrated that a sequential processing of EMI dynamic data via a Kalman filter (KF) and Extended Kalman filter (EKF) can be used to detect UXO and give good estimates of their positions and polarizabilities. The demonstration has been shown with data from two sensors, the MPV-II and the MetalMapper, in very different settings of dynamic data collection. The MPV-II, meant for hand-held operation, was used to interrogate a limited area within which a single target was present, akin to being waved by an operator in a detection mode. The MetalMapper instead was driven along adjacent 60-m long lanes to flag target locations across a large geographical area. In this latter configuration, multiple targets were present in the underground and sequentially appeared and disappeared from the field of view of the sensor as it was driven across the area. In both cases, the sensors operated in dynamic mode, meant for rapid land survey at the expense of data quality. Despite the noisy data, the KF-EKF algorithm was able to converge to proper solutions as verified independently either using our Gauss-Newton reference algorithm, using ground truth information whenever available, or comparing with independently obtained results.

An interesting intrinsic feature of the KF-EKF algorithm is its sequential processing of data as they become available. Hence, at every new data collection (e.g. new transmitter position), the algorithm updates the estimated parameters based on the newly computed Kalman gain. Such processing can be performed in less than 100 ms on a regular 2×2.8 GHz Quad-Core Intel Xeon computer, which is the real-time limit for our application. The inverted parameters include position, depth, and polarizabilities, albeit limited to the short data collection time range inherent to a dynamic survey. Yet, even if this dynamic data is not sufficient to perform classification, it is often sufficient to identify the subsurface anomaly as possible UXO or not, either based on simple signal correlation to a library or based on a volume estimate. The method can therefore be used in a land survey for real-time target mapping, flagging those locations to which the instrument needs to return for more exhaustive cued interrogation.

A current limitation of our algorithm is to consider the process of Eq. (2.1a) as a Markov process of order 1, i.e. that the state at instance k depends solely on the state at instance $(k-1)$. For UXO detection, however, where targets are by definition stationary, this can be a limiting assumption. For example, in an operating mode akin to that of the MPV-II in Chapter 3, multiple measurements are collected atop a single target. The polarizabilities are therefore best estimated by using all data points simultaneously in the inversion algorithm. This is the approach taken by our Gauss-Newton algorithm, whereby data from all grid points collectively contribute to the construction of the least-square problem from which a single position, depth, and polarizability set are obtained. The assumption of a Markov process of order 1 is therefore a restriction to using only one measurement set at each iteration, whereas all previous measurements atop the same target could be used. In a setting like that of the MetalMapper in Chapter 4, however,

the assumption is better justified since the sensor drives past large areas and is not continuously measuring on top of the same target. We therefore recommend the use of the present KF-EKF algorithm in this second setting, whereas a generalization to an order N Markov process should be implemented for the inversion of data collected atop a single target.

In addition, several avenues of follow on work could be proposed to the present work:

- **Integration to existing systems:** The present KF-EKF algorithm is currently not integrated with any sensor but stands alone and performs data processing off-line. The code is currently written in Matlab^{TM} and therefore requires the acquisition of a license in order to be executed. In order to perform a transfer of technology and incorporate the algorithm directly onto sensors for on-board real-time data processing, a few steps need to be undertaken: coordination with G&G Sciences Inc. to understand platform requirements, transcription of the code into an accepted language, on-board testing and adjustments, validation with existing data, further validation during data acquisition.

- **Real field validation:** Once on-board, the algorithm will need to be tested on a per-sensor basis (current versions have been validated off-line with the MPV-II and the MetalMapper). Further terrain validation with these sensors will be necessary, with comparison to ground truth whenever possible, or comparison with different methods otherwise (e.g. our Gauss-Newton algorithm or others).

- **Extension to new sensors:** New sensors are been actively developed in other SERDP programs, in particular the Pedemis [Barrowes 12] which is meant to be used in both static and dynamic modes. Owing to its geometry, the Pedemis can be viewed as an extension of the MetalMapper which could therefore be well adapted to a KF-EKF real-time processing (we showed in this work that a dynamic operation of the MetalMapper is well suited with the sequential processing feature of KF-EKF).

- **Optimized feedback information:** The GUI proposed in Section 4.4. is merely an illustration of a possible feedback to the operator, updated in real-time as data are processed sequentially. The proposed GUI not only displays information directly obtained from the KF-EKF algorithm (position, depth, polarizabilities), but also extrapolate additional information such as volume estimate, aspect ratio, and probability of being a target of interest based on a certain criterium. The latter should be further validated with real data in order to define thresholds of probabilities and optimized flagging system in order to reduce the rate of false alarms. The GUI should also be written in a language accepted by the sensors hardware.

- **Longer dynamic collection window:** The KF-EKF algorithm is more advanced than a simple detection algorithm since it provides an estimate of all the parameters of the dipole model, including the time dependent polarizabilities. The latter are currently limited to a window of 2.7 ms which is too short to attempt a reliable target identification. As a result, the polarizabilities are used merely to estimate target volume and aspect ratio. With little additional complexity, the collection window could be extended to 8 ms and the polarizability information could become much more valuable, opening the possibility of real-time target identification during data collection.

Bibliography

[Aliamiri 07] A.. Aliamiri, J.. Stalnaker & E.L. Miller. *Statistical Classification of Buried Unexploded Ordnance Using Nonparametric Prior Models*. IEEE Transactions on Geoscience and Remote Sensing, vol. 45, no. 9, page 2794, 2007.

[Barrowes 04] Benjamin E. Barrowes, Kevin O'Neill, Tomasz M. Grzegorczyk, Xudong Chen & Jin A. Kong. *Broadband Analytical Magnetoquasistatic Electromagnetic Induction Solution for a Conducting and Permeable Spheroid*. IEEE Trans. on Geosci. Remote Sens., vol. 42, no. 11, pages 2479–2489, November 2004.

[Barrowes 12] Benjamin E. Barrowes, Fridon Shubitidze, Tomasz M. Grzegorczyk, Pablo Fernandez & Kevin O'Neill. *Pedemis: a Portable Electromagnetic Induction Sensor with Integrated Positioning*. In Detection and Sensing of Mines, Explosive Objects, and Obscured Targets XVII, volume 8357, 2012.

[Bell 01] T. H. Bell, B. J. Barrow & J. T. Miller. *Subsurface discrimination using electromagnetic induction sensors*. IEEE Trans. on Geosci. Remote Sens., vol. 39, no. 6, pages 1286–1293, June 2001.

[Beran 11a] Laurens Beran, Stephen Billings & Doug Oldenburg. *Incorporating Uncertainty in Unexploded Ordnance Discrimination*. IEEE Transactions on Geoscience and Remote Sensing, vol. 49, no. 8, page 3071, 2011.

[Beran 11b] Laurens Beran, Stephen Billings & Doug Oldenburg. *Robust Inversion of Time-domain Electromagnetic Data: Application to Unexploded Ordnance Discrimination*. J. Environ. Eng. Geophysics, vol. 16, no. 3, page 127, September 2011.

[Bucy 68] R. S. Bucy & P. D. Joseph. Filtering for stochastic processes with applications to guidance. John Wiley & Sons, 1968. ISBN 0-8218-3782-6.

[Chen 07] Xudong Chen, Kevin O'Neill, Tomasz M. Grzegorczyk & Jin Au Kong. *Spheroidal Mode Approach for the Characterization of Metallic Objects Using Electromagnetic Induction*. IEEE Trans. on Geosci. Remote Sens., vol. 45, no. 3, pages 697–706, March 2007.

[Collins 02] Leslie M. Collins, Yan Zhang & Lawrence Carin. *Model-based statistical sensor fusion for unexploded ordnance detection*. In Geoscience and Remove Sensing Symposium (IGARSS), volume 3, pages 1556–1559, Toronto, Ont., Canada, 2002.

[Fernández 10] Juan Pablo Fernández, Fridon Shubitidze, Irma Shamatava, Benjamin E. Barrowes & Kevin O'Neill. *Realistic subsurface anomaly discrimination using electromagnetic induction and an SVM classifier*. EURASIP Journal on Advances in Signal Processing, vol. 210, 2010.

[Fernández 11] Juan Pablo Fernández, Benjamin E. Barrowes, Tomasz M. Grzegorczyk, Nicolas Lhomme, Kevin O'Neill & Fridon Shubitidze. *A Man-Portable Vector Sensor for Identification of Unexploded Ordnance*. IEEE Sensors Journal, vol. 11, no. 10, page 2542, 2011.

[George 11] David George & Fridon Shubitidze. *Correlation detection of targets from MetalMapper dynamic data*. Rapport technique, G&G Sciences Inc., September 2011. Project MR-1772.

[Gordon 02] M. Sanjeev Arulampalamand Simon Maskelland Neil Gordon & Tim Clapp. *A Tutorial on Particle Filters for Online Nonlinear/Non-Gaussian Bayesian Tracking*. IEEE TRANSACTIONS ON SIGNAL PROCESSING, vol. 2, no. 50, pages 174–188, February 2002.

[Grzegorczyk 08] Tomasz M. Grzegorczyk, Beijia Zhang, Jin Au Kong, Benjamin E. Barrowes & Kevin O'Neill. *Electromagnetic induction from highly permeable and conductive ellipsoids under arbitrary excitation – Application to the detection of unexploded ordnances*. IEEE Trans. on Geosci. Remote Sens., vol. 46, no. 4, pages 1164–1176, April 2008.

[Grzegorczyk 09] Tomasz M. Grzegorczyk, Benjamin Barrowes, Fridon Shubitidze, J. P. Fernandez, Irma Shamatava & Kevin O'Neill. *Detection of Multiple Subsurface Metallic Targets using EMI data*. In Proc. of SPIE, Detection and Sensing of Mines, Explosive Objects, and Obscured Targets, volume 73030T, 2009. Orlando, FL.

[Grzegorczyk 11] Tomasz M. Grzegorczyk, Benjamin E. Barrowes, Fridon Shubitidze, Juan Pablo Fernández & Kevin O'Neill. *Simultaneous Identification of Multiple Unexploded Ordnance Using Electromagnetic Induction Sensors*. IEEE Trans. on Geosci. Remote Sens., vol. 49, pages 2507–2517, July 2011.

[Hager 89] John W. Hager, James F. Behensky & Brad W. Drew. *The universal grids: Universal Transverse Mercator (UTM) and Universal Polar Stereographic (UPS)*. Rapport technique, Defense Mapping Agency, 1989.

[Hu 04] Wei Hu, Stacy L. Tantum & Leslie M. Collins. *EMI-based classification of multiple closely spaced subsurface objects via independent component analysis*. IEEE Trans. Geosci. Remote Sens., vol. 42, no. 11, pages 2544–2554, 2004.

[Jackson 99] J. D. Jackson. Classical electrodynamics. Wiley, third edition, 1999.

[Kalman 60] R. E. Kalman. *A New Approach to Linear Filtering and Prediction Problems*. Transactions of the ASME - Journal of Basic Engineering, vol. 82, pages 35–45, 1960.

[Kappler 11] Karl N. Kappler & Erika Gasperikova. *A Hybrid Method for UXO vs. Non-UXO Discrimination*. J. Environ. Eng. Geophysics, vol. 16, page 177, 2011.

[Kass 12] M. Andy Kass & Yaoguo Li. *Quantitative Analysis and Interpretation of Transient Electromagnetic Data via Principal Component Analysis*. IEEE Transactions on Geoscience and Remote Sensing, vol. 50, no. 5, page 1910, 2012.

[Kay 93] Steven M. Kay. Fundamentals of statistical signal processing – estimation theory. Prentice Hall Signal Processing Serries, 1993. ISBN 0-13-345711-7.

[Miller 01] Jonathan T. Miller, Thomas H. Bell, Judy Soukup & Dean Keiswetter. *Simple Phenomenological Models for Wideband Frequency-Domain Electromagnetic Induction*. IEEE Trans. on Geosci. Remote Sens., vol. 39, no. 6, pages 1294–1298, June 2001.

[Nelson 01] H. H. Nelson & J. R. McDonald. *Multi-sensor towed array detection system (MTADS) for UXO detection*. IEEE Trans. on Geosci. Remote Sens., vol. 39, no. 6, pages 1139–1145, June 2001.

[Nelson 07] H. H. Nelson, D. A. Steinhurst, B. Barrow, T. Bell, N. Khadar, B. SanFilipo & I. J. Won. *Enhanced UXO Discrimination Using Frequency-Domain Electromagnetic Induction*. Final report to the ESTCP program office (DOD) Arlington VA for project MM-0601, Naval Research Laboratory, 2007. Accession Number : ADA469893.

[Pasion 01a] Leonard R. Pasion & Douglas W. Oldenburg. *A Discrimination Algorithm for UXO Using Time Domain Electromagnetics*. J. Environ. Eng. Geophysics, vol. 6, page 91, 2001.

[Pasion 01b] Leonard R. Pasion & Douglas W. Oldenburg. *Locating and determining dimensionality of UXO using time domain electromagnetic induction*. J. Environ. Eng. Geophysics, 2001.

[Pasion 07] L. Pasion, S. Billings, D. Oldenburg & S. Walker. *Application of a library based method to time domain electromagnetic data for the identification of unexploded ordnance*. Journal of Applied Geophysics, vol. 61, no. 3-4, page 279, 2007.

[Prouty 09a] Mark Prouty. *Detection and Classification with the MetalMapper^{TM} at Former Camp San Luis Obispo – Draft Demonstration Plan*. Rapport technique, Geometrics Inc., March 2009. ESTCP Project No. MM-0603.

[Prouty 09b] Mark Prouty. *MetalMapper System: Camp San Luis Obispo Discrimination Study*. Final report to the ESTCP program office (DOD) Arlington VA for project MM-0603, ESTCP, 2009.

[Prouty 11] Mark Prouty, David C. George & D. D. Snyder. *MetalMapper: a multi-sensor TEM system for UXO detection and classification*. Rapport technique, ESTCP report, February 2011. Project 200603.

[Pulsipher 04] B. A. Pulsipher, R. F. O'Brien, R. O. Gilbert, D. J. Bates, J. E. Wilson, G. A. Sandness, N. L. Hassig & K. K. Anderson. *Statistical Methods and Tools for UXO Characterization*. Rapport technique, Strategic Environmental Research and Development Program, 2004.

[Ristic 04] Branko Ristic, Sanjeev Arulampalam & Neil Gordon. Beyond the Kalman filter: Particle filters for tracking applications. Artech House, 2004.

[Shubitidze 08] F. Shubitidze, D. Karkashadze, B. Barrowes, I. Shamatava & K. O'Neill. *A new physics based approach for estimating a buried object's location, orientation and magnetic polarization from EMI data*. J. Env. and Eng, Geophys., vol. 13, pages 115–130, 2008.

[Shubitidze 10] Fridon Shubitidze, David Karkashadze, Juan Pablo Fernández, Benjamin E. Barrowes, Kevin O'Neill, Tomasz M. Grzegorczyk & Irma Shamatava. *Applying a volume dipole distribution model to next-generation sensor data for multi-object data inversion and discrimination*. Proc. of SPIE, page 766407, 2010.

[Smith 90] Stanley O. Smith, 1990. http://earth-info.nga.mil/GandG/publications/tm8358.1/tr83581a.html.

[Song 09] Lin-Ping Song, Douglas W. Oldenburg, Leonard R. Pasion & Stephen D. Billings. *Transient electromagnetic inversion for multiple targets*. SPIE Proceedings, vol. 7303, May 2009.

[Stratton 41] J.A. Stratton. Electromagnetic theory. McGraw-Hill, 1941. ISBN 0-07-062150-0.

[Tantum 01] Stacy L. Tantum & Leslie M. Collins. *A Comparison of Algorithms for Subsurface Target Detection and Identification Using Time-Domain Electromagnetic Induction Data*. IEEE T. on Geoscience and Remote Sensing, vol. 39, no. 6, pages 1229–1306, June 2001.

[Ware 03] G. Ware. *Geonics EM63 multichannel EM data processing algorithms for target location and ordnance discrimination*. Rapport technique, Environmental Security Technology Certification Program, UX–0035, 2003.

[Won 99] I. J. Won, D. A. Keiswetter, D. R. Hansen, E. Novikova & T. M. Hall. *GEM-3: A monostatic broadband electromagnetic induction sensor*. J. Environ. Eng. Geophys., vol. 2, pages 53–64, 1999.

[Zhang 01] Zhong Qing Zhang & Qing Huo Liu. *Two Nonlinear Inverse Methods for Electromagnetic Induction Measurements*. IEEE Trans. on Geosci. Remote Sens., vol. 39, no. 6, pages 1331–1339, June 2001.

[Zhang 03] Y. Zhang, L. Collins, H. Yu, C. Baum & Lawrence Carin. *Sensing of unexploded ordnance with magnetometer and induction data: Theory and signal processing*. IEEE Trans. on Geosci. Remote Sens., vol. 41, pages 1005–1015, May 2003.